Carbohydrate Polymer Technologies and Applications 8 (2024) 100585

Contents lists available at ScienceDirect

Carbohydrate Polymer Technologies and Applications

journal homepage: www.sciencedirect.com/journal/carbohydrate-polymer-technologies-and-applications

Polyethylenimine functionalized graphene oxide and cellulose nanofibril composite hydrogels: Synthesis, characterization and water pollutants adsorption

Yufei Nan [a], Diego Gomez-Maldonado [a], Kailong Zhang [b], Haishun Du [c], Daniel C. Whitehead [d], Mi Li [b], Xinyu Zhang [c], Maria Soledad Peresin [a,*]

[a] *Sustainable Bio-Based Materials Laboratory, College of Forestry, Wildlife and Environment, Auburn University, 602 Duncan Drive, Auburn, AL 36849, USA*
[b] *Center for Renewable Carbon, School of Natural Resources, University of Tennessee Knoxville, Knoxville, TN 37996-4570, USA*
[c] *Department of Chemical Engineering, Auburn University, Auburn, AL 36849 USA*
[d] *Department of Chemistry, Clemson University, Clemson, SC 29634, USA*

ARTICLE INFO

Keywords:
Polyethylenimine functionalized graphene oxide
Cellulose nanofibril composite hydrogels
Adsorption
Adsorption isotherms
Polyethylenimine functionalization
Heavy metal ions

ABSTRACT

A stable 2,2,6,6-tetramethylpiperidine-1-yl)oxyl (TEMPO)-oxidized cellulose nanofibril (TCNF)/graphene oxide (GO)/polyethylenimine (PEI) composite hydrogel was synthesized by self-assembly instead of chemical cross-linking. Their chemical, morphology, surface, and mechanical properties were characterized and adsorption behavior for methyl blue (–) was systematically investigated in terms of the optimal GO content, pH effect, kinetics, and isotherm models. Additionally, to assess the adsorption capability of the TCNF/GO/PEI hydrogel for various contaminants, its effectiveness was also tested for methylene blue (+), Cu (II), and soybean oils. The maximum adsorption capability for the methyl blue (–) dyes increased from 3125 to 3962 mg/g when 13.3 % of GO was added. The adsorption capability for Cu (II) and soybean oils rose from 205.3 to 218.5 and 2.1 to 7.2 mg/g, respectively. The adsorption capability of optimized TCNF/GO/PEI hydrogel for a variety of contaminants was improved overall based on the increase of surface area, electrostatic interactions, and hydrophobic domains. Moreover, adding GO did not impact the adsorption mechanism but increased the external diffusion rate in the intraparticle diffusion model. This work provides a self-assembling route to TCNF/GO/PEI hydrogels with great potential for the removal of multiple water pollutants.

1. Introduction

Cellulose nanomaterial (CNM) and PEI composites (CNM-PEI) are widely applied in different fields such as paper making (Köklükaya, Carosio, & Wågberg, 2018; Wu et al., 2022), wastewater treatment (Fang, He, Dong, Yang, & Qin, 2022; Kim et al., 2022; Wang et al., 2022b; Wu, Tufa, Kwon, Choi, & Lee, 2023; Zhang, Wang, Makila, Willfor, & Xu, 2022b), drug release (He et al., 2020; Li et al., 2019; Liu et al., 2021; Wang et al., 2022a), sensing Li et al., 2022; Wang et al., 2023), heterogeneous catalysis (Riva, Lotito, Punta, & Sacchetti, 2022a; Riva, Nicastro, Liu, Battocchio, Punta, & Sacchetti, 2022b; Riva, Punta, & Sacchetti, 2020), and others. Among these applications, water remediation has attracted the most attention due to the excellent adsorption capability for water pollutants compared with other materials (Nan, Gomez-Maldonado, Whitehead, Yang, & Peresin, 2023a; Riva, Fiorati, & Punta, 2021; Liu et al., 2024; Qin et al., 2024; Yun et al., 2024). Existing research has primarily focused on the adsorption of CNM-PEI composites for specific and single classes of water pollutants, such as heavy metal ions (Kim et al., 2022; Liu, Jin, Ouyang, & Wang, 2017), toxic dyes, and other organic chemicals have been studied, and have shown superior adsorption performance and good regeneration ability. Additionally, CNM-PEI composite coated by graphene was also demonstrated with high efficacy for cleaning oil spills (Chatterjee, Ke, & Liao, 2020), underscoring the versatility of CNM-PEI materials in targeting single pollutants (Nan et al., 2023a).

However, real-world water resources such as rivers, lakes, and even oceans are polluted by a complex mixture of multiple pollutants, such as toxic metals, plastics, manufactured chemicals, petroleum, urban and industrial wastes, pesticides, fertilizers, pharmaceutical chemicals, agricultural runoff, and sewage (Escher, Stapleton, & Schymanski, 2020;

---

* Corresponding author.
E-mail address: soledad.peresin@auburn.edu (M.S. Peresin).

https://doi.org/10.1016/j.carpta.2024.100585

Landrigan et al., 2020; Yap et al., 2020). Addressing such diverse contamination requires a shift from targeting single pollutants to managing multiple pollutants simultaneously (Hlongwane, Sekoai, Meyyappan, & Moothi, 2019; Strokal et al., 2019). This necessitates the development of CNM-PEI composites that can efficiently adsorb a broad spectrum of contaminants. However, cellulose and PEI are hydrophilic; they are less effective against hydrophobic molecules, solvents, and oils. Thus, developing materials that enhance the hydrophobic adsorption capacity is essential for expanding their applications.

A promising approach to enhancing adsorption capacity involves incorporating adsorptive powders, such as graphene (Hou, Zhang, Li, & Wang, 2012), titanium dioxide, metal or metal oxide (Thoniyot, Tan, Karim, Young, & Loh, 2015), and biochar (Weerasundara, Gabriele, Figoli, Ok, & Bundschuh, 2021), into a tough hydrogel (Makhado, Pandey, Modibane, Kang, & Hato, 2020). Recently GO has emerged as a novel material for removing various contaminants from water resources (Yap et al., 2020; Zheng et al., 2021). GO is composed of a single or up to a few-layer graphene sheet with a high surface area (2600 m^2/g). This extensive surface area makes GO a highly effective material for the removal of oil, organic compounds, and metal ions from aqueous solutions (Yap et al., 2020). Furthermore, GO has abundant oxygen-containing functional groups, such as carboxyl, epoxy, keto, among others, which serve as active sites to further increase the adsorption capability for water pollutants (Jiang et al., 2019), while presenting good mechanical and chemical stability (Qiu, Wang, & Chen, 2022; Zheng et al., 2021). Several research studies have highlighted the effectiveness of GO as an excellent absorbent for wastewater treatment (Arshad, Selvaraj, Zain, Banat, & Haija, 2019; Yap et al., 2020; Zheng et al., 2021). GO can be chemically modified with various functional groups, such as amines, carboxyl, and hydroxyl groups, to alter its surface charges and hydrophobic properties for diverse applications. However, a major drawback of using GO as a neat material is its difficulty in separation from the aqueous medium, since GO disperses in water (Yap et al., 2020). To overcome this limitation, the GO needs to be immobilized on skeleton substrates to arrest the leaching of GO into water to help separate them from water after adsorption.

This work aims to incorporate GO into CNM/PEI composites to form a strong CNM/GO/PEI composite hydrogel for the removal of a variety of water pollutants. There are two methods to introduce GO into CNM/PEI composites (Ghasemlou, Daver, Ivanova, Habibi, & Adhikari, 2021; Liang, Bhagia, Li, Huang, & Ragauskas, 2020; Mariano et al., 2017; Tardy et al., 2017). Most reported studies focused on creating CNM/GO/PEI composites by covalent bond formation facilitated by the use of chemical crosslinkers, which usually cause secondary contamination and increase costs. The novelty of this work lies in creating a facile self-assembly route to incorporate GO into CNM-PEI composites mainly by physical interactions, resulting in the creation of a strong 3-D CNM/GO/PEI hydrogel. Furthermore, the adsorption of pollutants of different natures using the same material was tested in one study. Additionally, CNM isolated from a by-product from agricultural sources was used in the production of these hydrogels, showcasing a sustainable approach to waste valorization and water remediation. It was hypothesized that introducing GO into CNM/PEI composites would increase the diversity and effectiveness of contaminant adsorption due to the high surface area and oxygen groups on the GO.

To this end, TCNFs from soybean hulls were combined with GO by cationic chelation to form the TCNF/GO hydrogels and further functionalized in PEI solution by physical adsorption to form the TCNF/GO/PEI hydrogel. To test the adsorption capability of the resulting TCNF/GO/PEI hydrogels for multiple water pollutants, methyl anionic dyes, methylene blue cationic dyes, Cu (II) ions, and soybean oils were used as references. The reasoning behind the choice of pollutant relies on the nature of these pollutants with varying functional groups and hydrophobic domains. We based our choice on research existing in the literature to ensure that the results obtained can be directly comparable. Additionally, the chosen contaminants are representative of common pollutants encountered in industrial side streams and environmental settings, making these results even more relevant for real-world applications for water remediation strategies and pollution control. By doing this, soybean hulls were successfully valorized to a valuable TCNF/GO/PEI hydrogel in an easy self-assembling way and can be applied for the removal of various water pollutants examples to potentially help address the current and future environmental challenges.

2. Materials and methods

2.1. Chemicals and reagents

Cellulose nanofibrils (CNFs), (TEMPO)-oxidized cellulose nanofibrils (TCNFs), and GO were prepared at the Sustainable Bio-Based Materials Laboratory, Auburn University (Auburn, AL). Polyethylenimine (CAS number 9002-98-6, branched, Mw = 25,000 g/mol) was purchased from Sigma-Aldrich. (2,2,6,6-Tetramethylpiperidin-1-yl) oxyl (TEMPO) and methyl blue anionic dye from Alfa Aesar. Graphene flake (99.8 %) and anhydrous copper (II) sulfate (98 %) from Alfa Aesar. The soybean oil was supplied by Archer Daniels Midland company.

2.1.1. CNFs isolation

The CNF isolation processing was based on our previous research (Hernandez et al., 2022). 25 mL of 37 % w/w HCl was diluted to 3 L (0.3 %, 0.1 M) in a volumetric flask by the D.I. water, then transferred into a 3.7 L beaker. 150 g of soybean hulls (dry basis) was added into the beaker and hydrolyzed using a HCl solution at 90 ± 5 °C for 1 h using a magnetic stirrer at 190 rpm to remove pectin. The resulting fiber yield was 73 %. Afterward, samples were filtered without cooling using a Whatman #4 qualitative paper. The fibers were then thoroughly washed with deionized (DI) water using a centrifuge (Allegra 6 Centrifuge, Beckman Coulter, USA) at 3800 rpm to neutralize them. Next, 100 g of fibers (dry base) were added in 2.5 L of DI water with 56 g of $NaClO_2$ (80 % from Alfa-Aesar) and 15 mL of glacial acetic acid (99.9 % Fisher-scientific). Five doses of $NaClO_2$ and glacial acetic acid were added to complete the bleaching step at 1 h intervals. After that, the bleached pulp from soybean hulls was washed to neutral pH and diluted to 2 wt.% suspension and was then processed with Masuko supermasscollider (MKZA10-15 J, Masuko Sangyo Co. LTD, Japan) for 12 passes, with a final consistency of 2.12 wt.% at pH 5.8 (Fig. 1A).

2.1.2. TCNFs preparation

TCNFs were produced using TEMPO-mediated oxidation, following the procedure described in previous studies (Nan, Gomez-Maldonado, Iglesias, Whitehead, & Peresin, 2023b; Lu et al., 2020; Ono, Takeuchi, Zhou, & Isogai, 2021). 5 g of CNF (cellulose nanofibril) (dry mass basis) was dispersed in 500 mL of distilled water with TEMPO 0.08 g (0.1 mmol/g CNF) and NaBr 0.5 g (1 mmol/g CNF), and the pH was adjusted to 10 by adding 0.5 M aq. NaOH. Then, 30 mL of 12.5 % aq. NaClO solution was slowly added to the CNF slurry (1.66 mL/10 min, total 3 h) and the reaction mixture was maintained at pH 10.5 at 25±1 °C by adding aq. 0.5 M NaOH simultaneously. Next, the oxidized CNFs were precipitated by adding ethanol (1500 mL) and then centrifuged at 3800 rpm by centrifugation (Allegra 6 Centrifuge, Beckman Coulter, USA). Finally, the oxidized CNFs were washed thoroughly with distilled water and filtered using a 0.20 μm cellulose acetate filter paper (Fig. 1B).

2.1.3. GO preparation

GO preparation was adapted from the Hummers' method (Chen, Yao, Li, & Shi, 2013). In brief, 3 g of graphene flake (325 mesh) and 18 g of potassium permanganate were added in a 1 L flat-bottomed flask. The acid mix with 360 mL of 98 wt.% H_2SO_4 and 40 mL of 85 wt.% H_3PO_4, was slowly added to the flask. Then, the reaction system was placed in an oil bath at 50 °C and stirred at 500 rpm for 30 h. After that, the reaction solution was poured into a beaker with ice (formed by 500 mL DI water) and followed by a slow addition of 15 mL H_2O_2 (30 %) with a

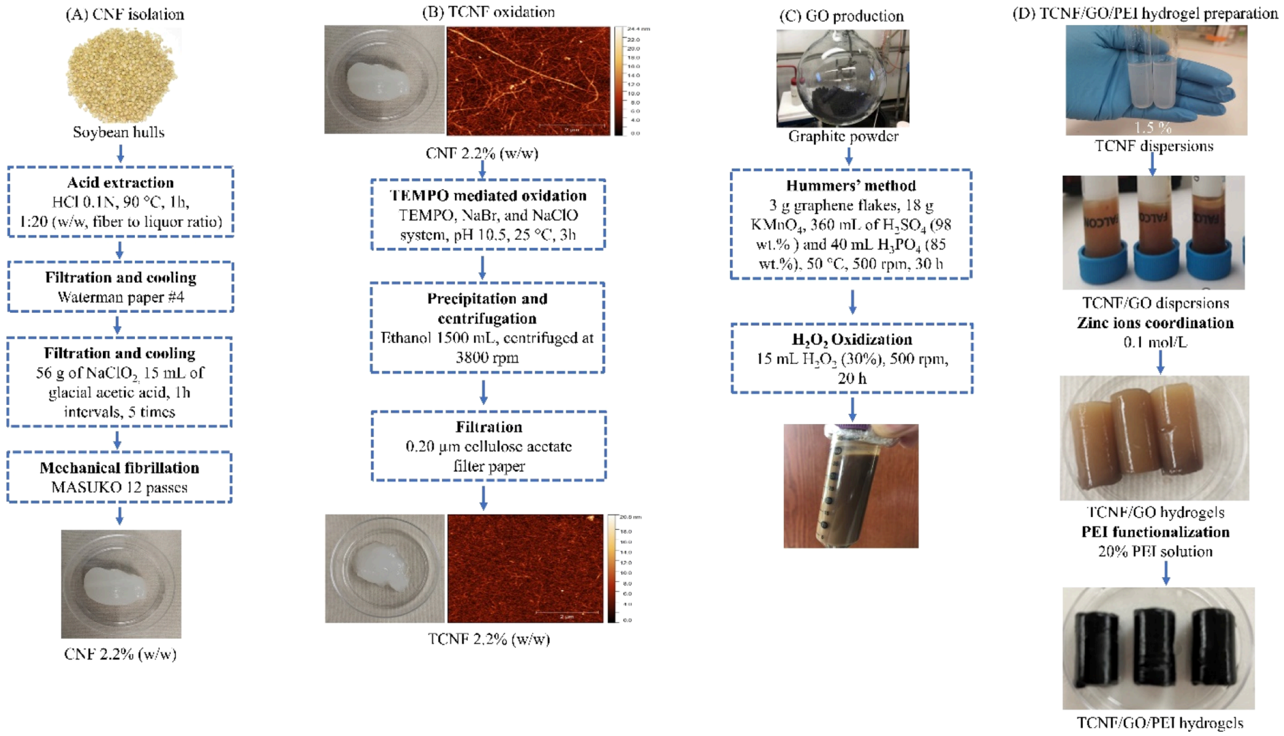

Fig. 1. The scheme of CNF isolation (A), TCNF production (B), GO production (C), and TCNF/GO/PEI hydrogels synthesis (D).

syringe. This caused the color of the solution to change from dark brown to yellow, and it was then stirred at 500 rpm for 20 h. Finally, the resulting solution was sequentially washed by DI water, hydrochloric acid (36–38 %), and ethanol by centrifuging at 6000 rpm to remove the metals and manganese chloride (Fig. 1C). The chemical reactions involved in GO oxidation are shown in Eqs. (1)–(3):

$$C + KMnO_4 + H_2SO_4 \rightarrow GO + MnO_2 + K_2SO_4 + H_2O \quad (1)$$

$$C_6H_6 + 3KMnO_4 + 6H_2SO_4 \rightarrow GO + 3MnO_2 + 3K_2SO_4 + 6H_2O \quad (2)$$

$$MnO_4^- + 8H^+ + 5e^- \rightarrow Mn2{+}{+}4H_2O \quad (3)$$

2.2. Synthesis of TCNF/GO/PEI hydrogels

TCNF/GO hydrogels were prepared by dropwise addition of a 20 wt.% aq. $ZnCl_2$ solution along the walls of the glass tube into a 1.5 wt.% aq. TCNFs dispersion containing 0 wt.%, 3.3, 6.7, and 13.3 wt.% of GO (all wt.% based on the TCNF). The final zinc ion concentration was controlled to be 0.1 mol/L. Then, the mixture was allowed to stand for 24 h at rest to enable the formation of the hydrogels. Afterward, the resulting hydrogel was rinsed with 150 mL DI water three times to remove unbound Zn^{2+} ions. Subsequently, TCNF/GO hydrogels were immersed in an aq. PEI solution with pH 11.6 at 25 ± 1 °C for 24 h for further functionalization. Finally, the unfunctionalized hydrogels were named TCNF, TCNF/3.3 %GO, TCNF/6.7 %GO, and TCNF/13.3 %GO (all % GO are expressed on TCNF basis), while the functionalized hydrogels were named TCNF/PEI, TCNF/6.7 % GO/PEI, and TCNF/13.3 % GO/PEI hydrogels, respectively. They were first placed into 150 mL anhydrous ethanol solution for 2 h and then were washed with 150 mL DI water approximately 5 times until the pH of the cleaning water remained neutral (Fig. 1D).

2.3. Materials characterization

2.3.1. Attenuated total reflectance-Fourier transform infrared spectroscopy (ATR-FTIR)

To confirm that GO and PEI were successfully introduced into the hydrogels, ATR-FTIR (PerkinElmer Spotlight 400 FT-IR Imaging System, Perkin-Elmer, USA) was used to test their corresponding functional groups in the hydrogels. Samples were freeze-dried at −50 °C for 48 h and then analyzed using a PerkinElmer Spotlight 400 FT-IR Imaging System. An attenuated total reflectance (ATR) accessory with diamond/ZnSe crystal was used for collecting 64 scans with 4 cm^{-1} resolution. Data was processed with Spectrum 6 Spectroscopy Software (PerkinElmer).

2.3.2. Raman spectroscopy

To further confirm the presence of GO in the TCNF/GO and TCNF/GO/PEI hydrogels, Raman spectroscopic analysis was carried out by DXR Raman Spectroscopy (Thermo Scientific, USA). A 532 nm (5 0.0 mW power) wavelength laser was used in the Raman spectrometer to analyze the sample. The data acquisition has been carried out in a range of 500–3500 cm^{-1} by OMNIC software.

2.3.3. Elemental analysis

To investigate the effect of GO content on the chemical composition of TCNF/GO/PEI hydrogels, elemental analysis was conducted to measure the carbon (C), nitrogen (N), and hydrogen (H) content. For each analysis, 2 mg of freeze-dried sample were used for elemental analysis by an elemental analyzer (Elementar vario MICRO, Ronkonkoma, NY, USA). Three replicates were performed for each sample.

2.3.4. Scanning electron microscopy (SEM)

SEM was used to observe the morphological properties. Freeze-dried samples were set onto aluminum studs and sputtered with gold for 90 s in an EMS × 550 Sputter Coating Device from Science Services (Munich, Germany). Images with magnifications of ×100 were recorded in a Zeiss Evo 50VP SEM (Oberkochen, Germany).

2.3.5. *Inverse gas chromatography-surface energy analyzer (IGC-SEA)*

The surface energy analyses and Brunauer–Emmett–Teller (BET) specific surface area measurements were conducted using IGC-SEA (Surface Measurement Systems, UK). Each sample (20–50 mg) was packed into a 4 mm chromatographic column and conditioned under a nitrogen gas flow for 2 h. The dispersive components of the surface energy were measured using n-alkanes probes, including octane, nonane, decane, and undecane. The acid-base components of the surface energy were determined using ethyl acetate and dichloromethane as probes. All measurements were carried out under controlled conditions (30 °C, 0 % relative humidity (RH)). The BET specific surface areas (SBET) were determined by calculating the isotherm of octane with a pressure ratio (P/P0) ranging between 0.05 and 0.35.

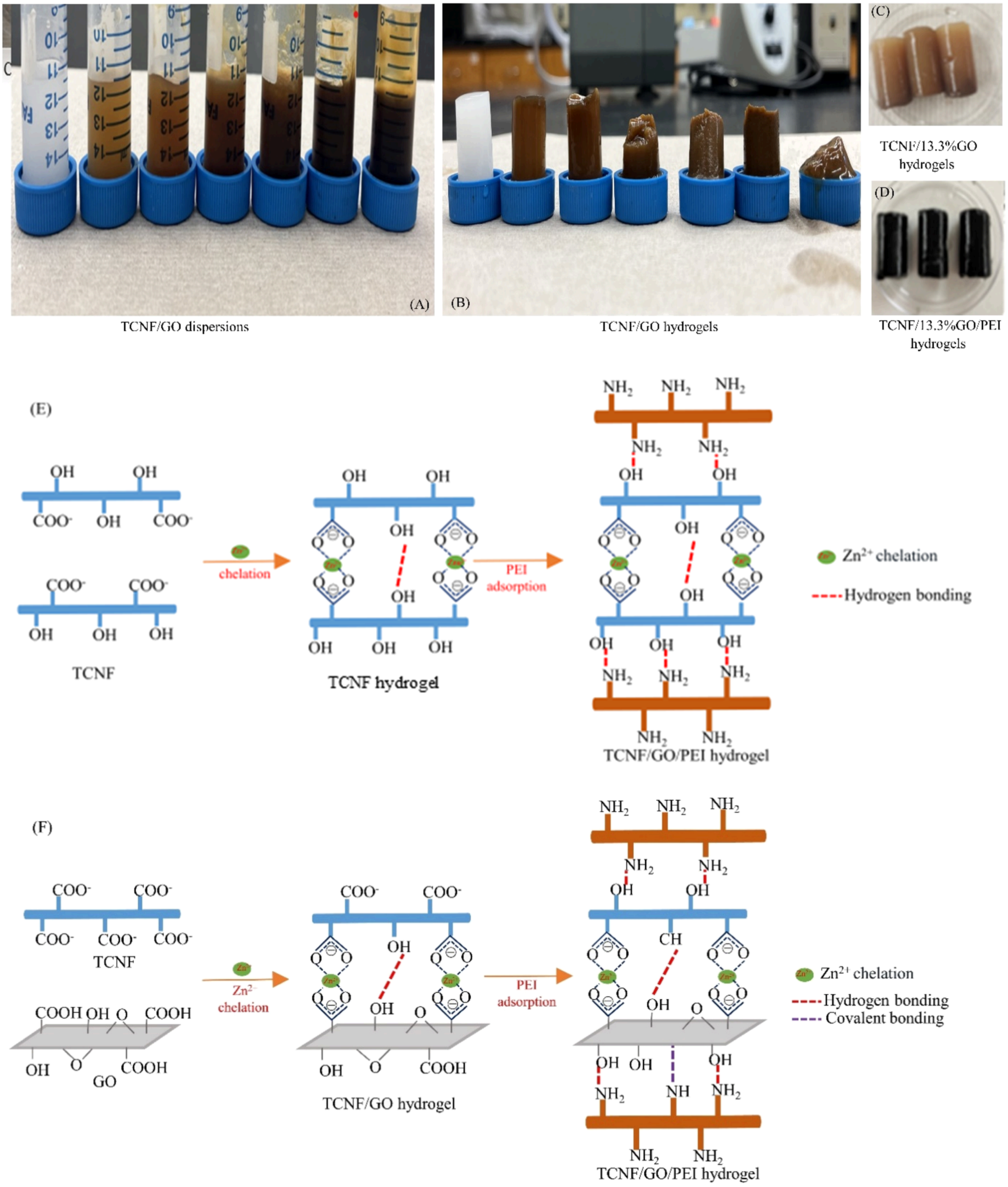

Fig. 2. Images of TCNF/GO dispersions (A) and TCNF/GO hydrogels with different concentrations of GO (from left to right: 0 % GO, 6.7 % GO, 13.3 % GO, 33.3 % GO, 66.7 % GO, 100 % GO with 1.5 % TCNF, 1.5 % GO without TCNF (B)) chelated by cationic ions; TCNF/13.3 % GO hydrogels (C) and TCNF/13.3 % GO/PEI hydrogels (D). Illustration of the chemical reactions and physical interactions involved in the formation of TCNF/PEI (E) and TCNF/GO/PEI (F) hydrogels.

2.3.6. *Compressive mechanical strength test*

To investigate the effect of the addition of GO in the mechanical properties of the formed composites, unconfined, uniaxial compression tests were measured using a universal testing machine Dynamic Mechanical Analyzer (DMA) (TA Instruments RSA 3, TA Instruments, IL, USA). Prior to analysis, all of the hydrogels were submerged in DI water for 24 h before analysis. Then, hydrogels were cut into disc shapes with diameters of 25 mm and heights of 6 mm. Tests were performed on the multiple extension mode test with 25 mm diameter parallel plate compression geometry at a speed 0.02 mm s^{-1} under 25±1 °C.

2.4. *Adsorption behaviors*

2.4.1. *Effect of GO content and retention time*

Hydrogels with varying concentrations of GO were cut into a 3.5 mm long cylinder (0.0186 g dry basis) and then immersed into 10 mL of 200 mg/L methyl blue buffer solutions with a pH range from 2.7 to 7.7 and left at rest at 25 ± 1 °C. The concentrations of methyl blue dye in the supernatant were quantified by UV spectroscopy (Genesys 50 UV–visible Spectrophotometer, Thermo Scientific, Waltham, MA, USA) at 596 nm at different times.

2.4.2. *Adsorption kinetics*

A 3.5 mm long cylinder (0.0186 g) of hydrogel was added to 10 mL 200 mg/L methyl blue solution at pH 5.7 and 25 °C, until the adsorption reached an equilibrium. Aliquots were taken at set time periods to obtain the concentration remaining in the solution. The adsorption capacities were calculated with the following equations:

$$q_{t=}\frac{C_0 - C_t}{\mathrm{m}}V \tag{4}$$

$$q_{e=}\frac{C_0 - C_e}{\mathrm{m}}V \tag{5}$$

where C_0 (mg/L) and C_t (mg/L) are the initial and concentrations after t time, respectively; q_t (mg/g) is the adsorption capacity at time t; V (L) represents the solution volume of methyl blue, and m (g) represents the dry mass of the hydrogel adsorbent; Ce (mg/L) are equilibrium concentrations; q_e (mg/g) is the adsorption capacity at equilibrium.

The adsorption data were then fitted to the pseudo-first-order and pseudo-second-order kinetic model as well as intra-particle diffusion model, using the equations presented below:

$$Ln(q_{e-}q_t) = Lnq_e + k_1\mathrm{t} \tag{6}$$

$$\frac{t}{q_t} = \frac{t}{k_2 q_e^2} + \frac{t}{q_e} \tag{7}$$

$$q_t = K_{id}t^{0.5} + c \tag{8}$$

where k_1 and k_2 are the rate constants for the pseudo-first-order adsorption and pseudo second-order adsorption kinetic models, respectively. K_{id} is the rate constant (g mg^{-1} min^{-1}) of intra-particle diffusion kinetics, c is the intercept.

2.4.3. *Adsorption isotherms*

0.0186 g absorbent was immersed in 10 mL methyl blue dye solutions with concentrations from 20 to 70,000 mg/L to study the adsorption isotherm. The adsorption experiments were carried out at 25 °C at an initial pH of 5.7 after 120 h. The adsorption values were fitted into linear (Eq. (9)) and non-linear (Eq. (10)) Langmuir isotherm models. Additionally, the data was fitted into linear (Eq. (12)) and non-linear (Eq. (13)) Freundlich isotherm models to describe its behavior. The equations used are described below:

$$\frac{C_e}{q_e} = \frac{C_e}{q_m} + \frac{1}{K_L q_m} \tag{9}$$

$$q_e = \frac{q_m K_L C_e}{1 + K_L C_e} \tag{10}$$

$$R_L = \frac{1}{1 + K_L C_0} \tag{11}$$

where q_m (mg g^{-1}) is the maximum adsorption capacity estimated by the Langmuir model, and K_L (L mg^{-1}) is Langmuir constant which is related to the adsorption intensity (Guo et al., 2018). R_L is the separation factor, which values indicate the adsorption to be unfavorable when $R_L > 1$, linear when $R_L = 1$, favorable when $0 < R_L < 1$, and irreversible when $R_L = 0$. $C_{0_\circ}$ refers to the initial concentration of the adsorbate in (mg/L)

$$Lnq_e = LnK_F + \frac{LnC_e}{\mathrm{n}} \tag{12}$$

$$q_e = K_F c_e^{1/n} \tag{13}$$

K_F are constants of the Freundlich equations; 1/n in the Freundlich model represents an empirical parameter, which is related to the energetic heterogeneity of the adsorbent surface and determines either the favorable or unfavorable curve. When 1/n is greater than zero ($0 < 1/n < 1$) the adsorption is favorable, when 1/n is greater than 1, the adsorption process is unfavorable, and it is irreversible when $1/n = 1$.

2.4.4. *Adsorption capability for various pollutants*

The adsorption capability of the hydrogels for cationic methylene blue dyes, Cu (II) ions and soybean oils was also tested. The hydrogels 0.0186 g (dry basis) were immersed into 10 mL of 200 mg/L methylene blue buffer solutions with pH 5.7 and left to rest. Samples were collected at different time intervals (3, 6, 12, 24 h). Methylene blue concentrations in the supernatant were calculated using a UV spectrophotometer at 664 nm, respectively. Similarly, hydrogel cylinders of the same size were placed into 10 mL of 320 mg/L Cu (II) solutions for 24 h. The remaining Cu (II) ions in solution after hydrogel treatment were quantified by Inductively Coupled Plasma-Mass Spectrometry (ICP-MS). Finally, the same size of hydrogels was immersed in 5 g (W1) of pure soybean oil after 30 min, then removed hydrogels and tested the weight of oil left in the container (W_2). The soybean oil adsorption efficiency was calculated based on the following (Eq. (14)):

$$\text{Soybean oil adsorption efficiency}(\%) \times 100 \tag{14}$$

3. Results and discussion

3.1. *The effect of GO concentration on the stability of TCNF/GO hydrogels*

The carboxyl groups in TCNF can be chelated by cations to form stable white hydrogels (Fig. 2(A) and (E)) (Dong, Snyder, Williams, & Andzelm, 2013; Nan, Gomez-Maldonado, Iglesias, et al., 2023). In this work, GO was introduced into the TCNF dispersions and chelated by Zn^{2+} to form TCNF/GO hydrogels with a brown shade (Fig. 2(A) and (F)). The interaction promoting the hydrogel formation was based on the existence of similar carboxyl groups in GO that resulted in a stable TCNF/GO hydrogel when the GO concentration was less than 13.3 wt.% (Fig. 2(B)). However, a higher concentration of GO resulted in a collapse of the structure. After PEI functionalization, the color of TCNF/GO hydrogel changed from brown to black, likely induced by the GO reduction to graphene (Fig. 2(C) and (D)) (Geng, Yin, Liang, Zhu, & Luo, 2019), which will be further confirmed by the FTIR in the following section. Another visible change was that the material seemed stiffer after PEI functionalization due to the hydrogen bonding between abundant hydroxyl group in TCNF and GO with amine groups in PEI as well as PEI chemically reacts with oxygen-containing functional groups like epoxy, carbonyl in GO (Fig. 2(F)).

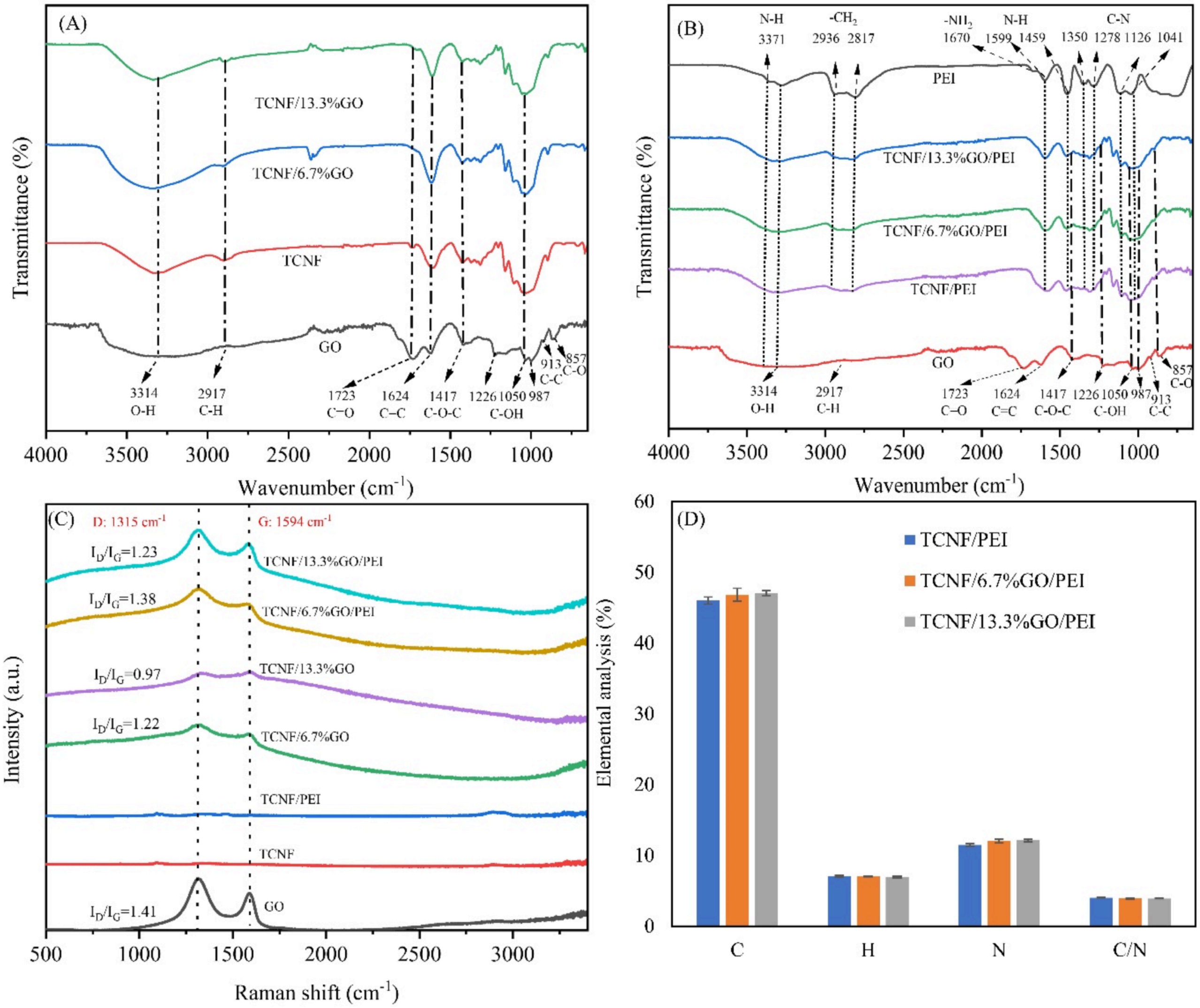

Fig. 3. FTIR spectra of GO, TCNF and TCNF/GO hydrogels (A), as well as PEI, GO and TCNF/GO/PEI hydrogels (B). Raman spectra of GO, TCNF/GO hydrogels, and TCNF/GO/PEI hydrogels (C); elemental analysis of TCNF/PEI and TCNF/GO/PEI hydrogels (D).

3.2. *Characterization of the hydrogels*

3.2.1. *Chemical properties*

FTIR spectra was used to identify the functional chemical group in PEI, GO, and corresponding hydrogels (Fig. 3). For the GO (Fig. 3(A)), the band at around 3400 cm^{-1} is related to O—H stretching vibration, 2917 cm^{-1} corresponds to the symmetric stretching vibration of C—H, 1723 cm^{-1} represents C═O stretching vibration in carboxyl group and the band at 1624 cm^{-1} corresponds to the skeletal stretching of C═O alkene group, C—O—C bending vibrations at 1417 cm^{-1} (Aliyari, Alvand, & Shemirani, 2016; Nikkhah, Tahermansouri, & Chekin, 2018). 1226, 1050 and 987 cm^{-1} are C—OH stretching/bending vibrations. Additionally, C—C and C—O bands are observed around 913 and 857 cm^{-1} (Mondal & Srivastava, 2020). The high intensity of major bands in GO revealed that large amounts of oxygen-containing groups are present after the oxidation process (Chaiyakun et al., 2012; Ruiz et al., 2019; Sharma et al., 2017). For PEI (Fig. 3(B)), the signals at 2936 and 2817 cm^{-1} correspond to the characteristic bands of —CH$_2$ stretching vibrations, while the bands at 1670 cm^{-1} and 1050 cm^{-1} correlated to the —NH$_2$ stretching vibrations, and C—C skeleton vibration, respectively (Papavlu, Dinca, Filipescu, & Dinescu, 2017). Furthermore, the band near 1599 cm^{-1} and 1459 cm^{-1} are the N—H bending vibration of primary amines in PEI; 1350, 1278, 1126, and 1041 cm^{-1} are C—N stretching vibrations (Pang et al., 2011). After PEI functionalization, some of GO characteristic peaks (1417, 1226, 987, 913, and 1050 cm^{-1}) were visible in the TCNF/6.7 %GO and TCNF/13.3 %GO hydrogel spectra, indicating GO was successfully introduced into the hydrogels (Fig. 3(A)). However, these signal bands become weakened. Some of the GO signal bands (1723, 1624, 913 cm^{-1}) disappeared after PEI functionalization. The weakened or disappearing bands for oxide-containing groups in TCNF/GO/PEI hydrogels indicate that reductive PEI could partially reduce GO to graphene (Fig. 3(B)) (Geng et al., 2019). All characteristic bands of PEI were observed in PEI functionalized hydrogels, proving the successful introduction of PEI to TCNF/PEI hydrogels.

To further confirm that GO or graphene exists in the TCNF/GO and TCNF/GO/PEI hydrogels, all samples were tested by Raman spectroscopy, as shown in Fig. 3(C). GO, TCNF/GO, and TCNF/GO/PEI hydrogels exhibit peaks at ~ 1315 cm^{-1} (D band) and ~1594 cm^{-1} (G band) corresponding to sp^3 disordered carbon and sp^2 hybridized carbon, respectively (Ding et al., 2014; Mondal & Srivastava, 2020). In comparison with GO, the D and G bands did not shift in hydrogels, but several changes occurred in the D and G peaks of the TCNF/GO and TCNF/GO/PEI hydrogels. Both D and G bands in TCNF/GO and TCNF/GO/PEI hydrogels become broader than those of GO. Additionally, the D and G bands became narrower when GO increased from 6.7 % to 13.3 %. However, both D and G bands in TCNF/GO/PEI hydrogels

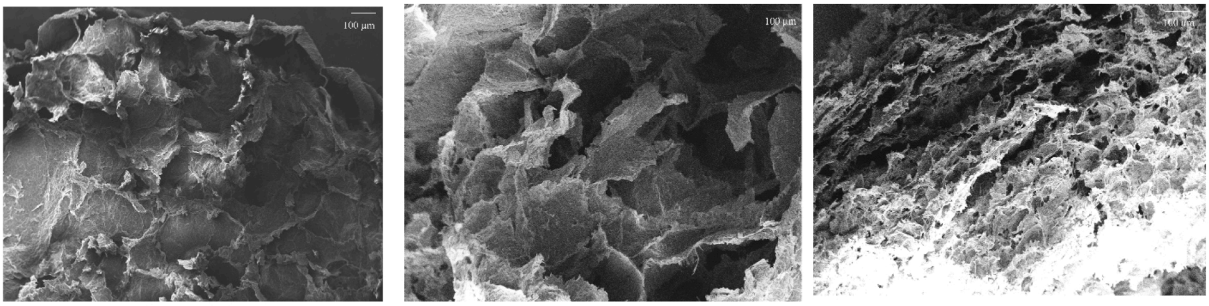

(A) TCNF hydrogel (B) TCNF/6.7% GO hydrogel (C) TCNF/13.3% GO hydrogel

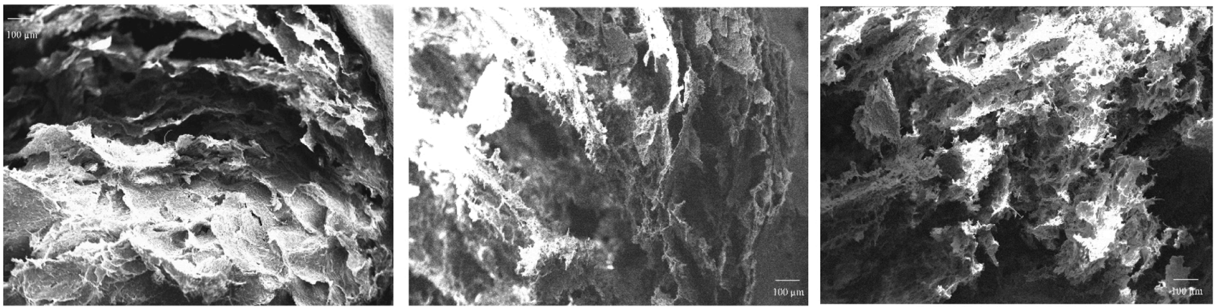

(D) TCNF/PEI hydrogel (E) TCNF/6.7% GO/PEI hydrogel (F) TCNF/13.3% GO/PEI hydrogel

Fig. 4. SEM images of TCNF, TCNF/GO, and TCNF/PEI hydrogels were all collected at 100x magnification.

became narrower after PEI functionalization compared with TCNF/GO hydrogels. To explain this, the intensity ratio of the D and G bands (I_D/I_G) has been used to find out the sp^2 domain size and partially ordered crystal structure of carbon, respectively. The ratio of I_D/I_G of GO is 1.41, it decreased to 1.22 and 0.97 in the TCNF/6.7 %GO and TCNF/13.3 %GO hydrogels, respectively. It indicates that TCNF has repaired the structural defects on the surface of GO, thus reducing the I_D/I_G (Yu et al., 2022). It seems 1.5 % of TCNF can repair more than 13.3 % of GO, as evidenced by a higher shift of I_D/I_G ratio in TCNF/13.3 %GO hydrogel. However, the I_D/I_G ratio increased to 1.23 and 1.38 after PEI functionalization. This indicates that PEI functionalization can increase the amount of graphite edges due to the reduction of GO (Liu, Guo, Zhou, & Qian, 2020).

The chemical composition of TCNF/GO/PEI hydrogels was performed to test the C, H, O, and N content in the hydrogels and shed light on the effect of GO addition in their chemical composition (Fig. 3(D) and Table S1). The N and C content increased from 11.48 % and 45.9 % to 12.1 % and 46.8, respectively, when the GO content increased from 0 % to 13.3 %. Furthermore, C/N significantly decreased from 4.0 % to 3.9 % (P-value <0.05), confirming that more PEI was adsorbed on the TCNF/GO/PEI hydrogel with increased GO content.

3.2.2. *Morphology characterization*

Morphologies were observed by SEM (Fig. 4). The TCNF hydrogel presented a dense structure (Fig. 4(A)). The addition of GO induces the change of morphologies of the hybrid aerogels, and the degree of the variation is dependent upon GO content (Nguyen et al., 2021). TCNF/6.7 % GO hydrogels showed a big pore size of porous 3D structure (Fig. 4B and D). However, TCNF/13.3 % GO hydrogel (Fig. 4(C)), despite the 3D structure of the TCNF, GO formed a small pore structure by aggregation of adjacent GO sheets. After further functionalization with PEI, TCNF/PEI hydrogel presented a scale-like porous structure. For TCNF/GO/PEI hydrogels, scale-like porous structures were partly covered by the GO aggregation and formed small pore-size 3D structures. However, compared with TCNF/13.3 % GO hydrogel, GO formed a 3D small porous structure that was unevenly arranged and seems to be affected by PEI (Fig. 4E and F) (Wei et al., 2017). To further confirm this, the surface area of those materials was tested (see next section).

Table 1
BET specific surface area (), mean value of dispersive surface energy (), specific surface energy (), total surface energy (), and polarity index (/) at 30 °C.

	(m^2/g)	mJ/m^2	mJ/m^2	mJ/m^2	/
TCNF	5	41.98	2.41	44.69	0.05
TCNF/3.3 %GO	5.31	55.85	6.92	62.45	0.11
TCNF/6.7 %GO	5.76	55.12	7.96	62.98	0.13
TCNF/13.3 %GO	3.74	44.76	4.22	49.11	0.09
TCNF/PEI	2.82	84.20	19.09	102.87	0.19
TCNF/3.3 %GO/PEI	3.21	66.41	8.47	74.98	0.11
TCNF/6.7 %GO/PEI	3.78	87.91	17.84	105.70	0.17
TCNF/13.3 %GO/PEI	4.18	52.27	5.53	60.8	0.21

3.2.3. *Surface area and surface energy*

SEM images in Fig. 4 demonstrated changes in morphology caused by GO and PEI functionalization. To quantify these changes, BET surface area measurements were performed. As shown in Table 1, compared with TCNF hydrogel (5.0 m^2/g), the surface area of TCNF/GO hydrogels increased with the increase of GO content, up to 5.8 m^2/g when GO content increased to 6.7 %, then decreased to 3.7 m^2/g when the GO content was increased to 13.3 %. The decrease of the surface area is possibly attributed to the aggregation of adjacent GO sheets resulting in small pore size 3D structure occurring, which has been observed by SEM (Wei et al., 2017). This indicated that low GO content ($\leq$6.7 %) can help to increase the surface area of TCNF hydrogels. However, the surface area of TCNF/PEI hydrogel decreased to 2.82 m^2/g. It means PEI functionalization caused a significant decrease in surface area, which was mainly caused by strong hydrogen bonding between TCNF and PEI. Interestingly, it was found that the surface area of TCNF/GO/PEI hydrogel increased from 2.82 to 4.78 m^2/g when GO content increased from 0 % to 13.3 %, which suggested that adding GO into the TCNF/PEI hydrogels can help prevent surface area loss of TCNF hydrogel directly functionalized by PEI. This may be due to PEI avoiding the accelerated gelation process achieved by the contact of adjacent GO sheets.

IGC-SEA was utilized to investigate the impact of surface modification and composite formation on the surface energy of the hydrogels, and how these changes in energy profiles influence the final adsorption properties and mechanism of the composites. Dispersive surface energy

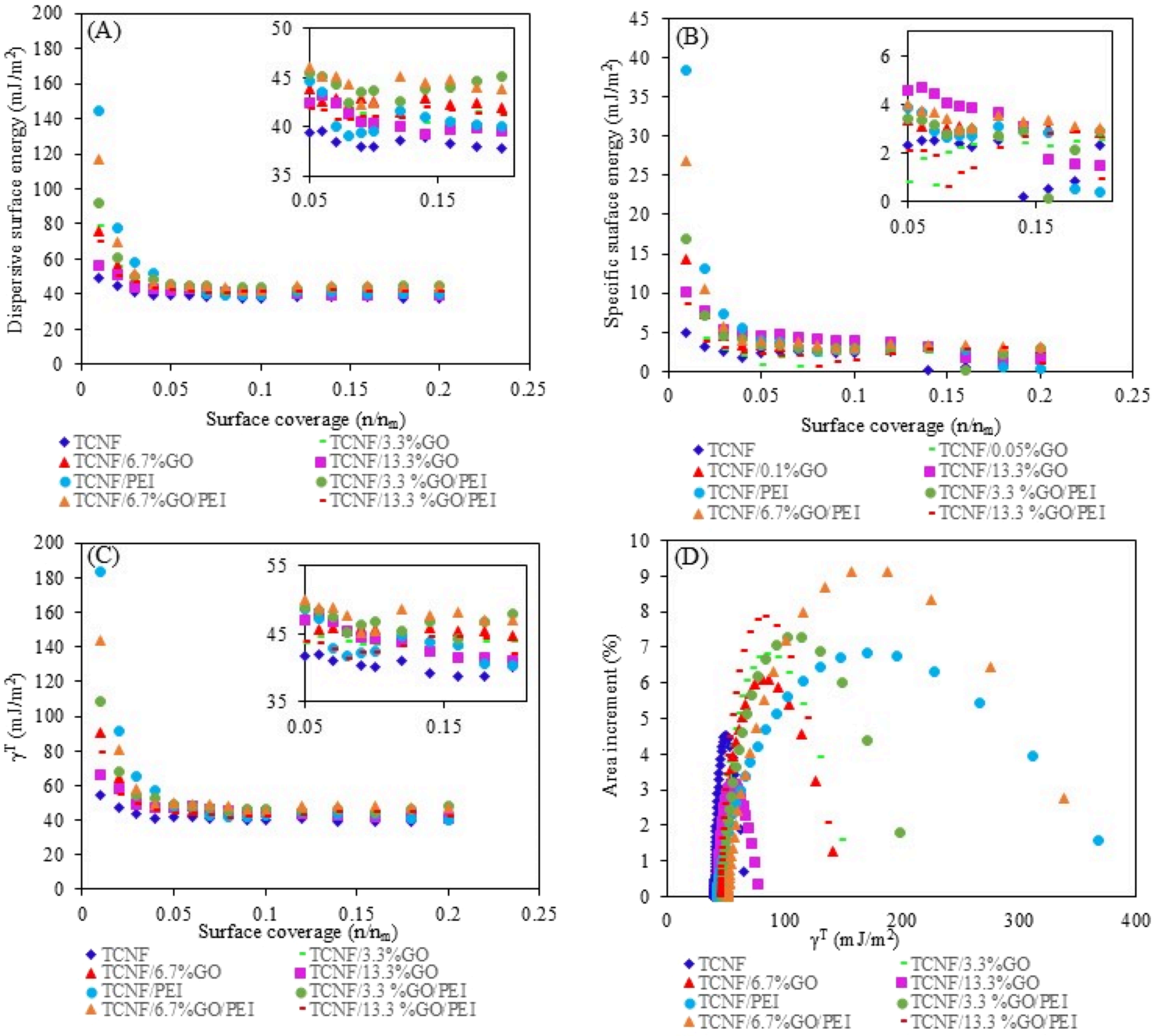

Fig. 5. Surface energy (A): γ^D, dispersive energy, (B): γ^{AB}, specific energy, (C): γ^T, total energy (γ^T=: $\gamma^D_+\gamma^{AB}$), (D): distribution of γ^T tested by IGC-ESA.

(γ_S^D) is determined by the retention of n-alkane probes in a highly diluted state. Dispersive interactions (apolar), also known as Lifshitz− van der Waals interactions, consist of London, Keesom, and Debye interactions. Conversely, specific (acid-base) surface energy (γ_S^{AB}) stems from interactions related to the solid's electron-accepting (Lewis's acid) and electron-donating (Lewis's base) capabilities. Specific interactions (polar) explain all other types of interactions, such as acid−base interactions, hydrogen bonding, or π bonding (Yao et al., 2015). The total surface energy (γ_S^T) is composed of γ_S^D, and γ_S^{AB}components. Fig. 5(A)–(C) show the γ_S^D, γ_S^{AB} and γ_S^T of studied hydrogels as a function of surface coverage (n/nm). Table 1 shows the mean value of surface energy determined at 50 % surface energy coverage. All samples exhibited significantly higher dispersive surface energy (γ_S^D) in comparison to specific surface energy (γ_S^{AB})indicating that dispersive surface energy had a predominant influence on these samples. The result revealed that the potential for physisorption was higher than that of chemisorption (Pal et al., 2019; Yao et al., 2015). Moreover, these values decrease significantly with increasing surface coverage at lower coverage levels, indicating that the samples are energetically heterogeneous. This heterogeneity is further confirmed by the distribution of γ_S^T (Fig. 5(D)), with a larger distribution being more energetically heterogeneous.

Compared with TCNF hydrogels, all functionalized hydrogels with GO or PEI presented higher $\gamma_S^D$and γ_S^{AB} as well as γ_S^T (Fig. 5(A) and (B)) and Table 1), which means all these modifications increased the surface energy of TCNF hydrogels. The mean value of $\gamma_S^D$and γ_S^{AB} as well as γ_S^T TCNF/GO hydrogels increased from 42.0, 2.4, and 44.7 (TCNF hydrogels) to 55.1, 8.0, and 62.5 mJ/m^2 when the GO content was 6.7 %, then decreased to 44.8, 4.2 and 49.1 mJ/m^2, respectively when the GO continued to being increased to 13.3 % at lowest surface coverage (Fig. 5 (C)). When these hydrogels were further functionalized by PEI, TCNF/PEI hydrogel showed the highest $\gamma_S^D$and γ_S^{AB} as well as γ_S^T (84.2, 19.1, and 102.9 mJ/m^2), then decreased when GO was introduced into the TCNF/PEI hydrogel and decreased to 55.2, 5.5 and 60.8 mJ/m^2 when the GO content increased to 13.3 %.

This result indicates that low levels of GO (less than 6.7 %) functionalization can enhance the surface energy of TCNF hydrogel, which is consistent with the changes observed in surface area after functionalization with GO. The presence of PEI on the surface significantly increases the surface energy of TCNF hydrogels, contrary to the change in surface area after PEI functionalization. However, the addition of GO to TCNF hydrogels followed by PEI functionalization leads to a decrease in surface energy, also contradicting the change in surface area. Therefore,

Table 2
The compressive mechanical properties of all hydrogels were investigated in compressive tests by DMA.

Hydrogels	Max stress (Kpa)	Fracture strain (%)	Compression modulus ((Kpa))
TCNF	17.1 ± 1.1	88.4	0.32
TCNF/6.7 %GO	10.4 ± 1.0	79.9	0.18
TCNF/13.3 %GO	5.4 ± 1.1	75.5	0.09
TCNF/PEI	38.6 ± 0.6	84.6	0.17
TCNF/6.7 %GO/PEI	48.7 ± 2.8	94.5	0.26
TCNF/13.3 %GO/PEI	40.9 ± 5.8	82.6	0.19

it appears that there is no clear relationship between surface area and surface energy, contrary to previous research findings (Bai et al., 2023). Meanwhile, compared to TCNF hydrogel, all functionalized hydrogels showed a broader distribution profile of total surface energy (Fig. 5(D)), which indicated that they had a large surface heterogeneity due to their complex physical structure (more porous) and chemical composition (new functional groups were introduced into the TCNF hydrogel). Among them, TCNF/PEI hydrogel displays the broadest distribution profile and the highest γ_S^T. It is worth noting that the order of the distribution profiles of all the hydrogels, from broadest to narrowest, coincides with the order of their surface energy, from highest to lowest. Hence, a higher surface energy corresponds to a larger surface heterogeneity (Bai et al., 2023; Hwang, Kim, Lee, & Park, 2023).

Additionally, the polarity index (γ_S^{AB}/γ_S^T) indicates the contribution of the polar components to the total surface energy, which is related to the hydrophilic properties of hydrogels. Compared with TCNF hydrogel, the polarity index of TCNG/GO hydrogel initially increased with an increase in GO content, reaching 0.13 when GO content increased to 6.7 %. After that, the polarity index of TCNG/GO hydrogel decreased as the GO content continued to increase, reaching 0.09 when GO content increased to 13.3 %. This change is caused by the change of active sites with the change in surface area. When these hydrogels were further functionalized by PEI, the polarity index of TCNF/PEI hydrogel was 0.19, which was higher than all GO functionalized hydrogels, indicating that PEI functionalized introduced more acid-base groups, making it more hydrophilic. However, the polarity index of TCNF/0.5 %GO/PEI hydrogel decreased to 0.11 due to the decrease in acid-base groups caused by reactions of the amine group in the PEI with the oxygen-containing groups in the GO. Subsequently, the polarity index of TCNF/GO/PEI hydrogel increased with continuing increase of GO content, reaching 0.21 when GO content went up to 13.3 % because extra GO introduced more electron-accepting (Lewis's acid) and electron-donating (Lewis's base) groups.

3.2.4. Compression properties

The mechanical properties of all hydrogels were investigated though compressive tests, and the results are summarized in Table 2. The compressive stress, compression modulus, and fracture strain of the TCNF hydrogel were found to be 17.1 Kpa, 0.32 Kpa, and 88.4 %, respectively. The mechanical properties decreased with GO additions of more than 6.7 %, declining to 5.4 Kpa, 0.09 Kpa and 75.5 %, respectively, when GO content researched to 13.3 %. These results indicate that GO content higher than 6.7 % does not contribute to increase the strength and toughness. These findings contrast with a previous study, which indicated that compressive stress of double-crosslinked cellulose–GO nanosheet composite hydrogel is higher than that of pure cellulose hydrogel when the GO content was 8 % (Wei, Wang, Xie, & Cai, 2022). Additionally, Zhang et al. reported that the optimal GO content for achieving the highest compressive stress in microcrystalline cellulose/GO composites crosslinked by epichlorohydrin is 0.2 wt.% (Zhang, Yang, & Liu, 2018), while Wei et al. showed that is 2 wt.% in cellulose-GO composites crosslinked by epichlorohydrin (Wei et al., 2022). These wide range of values may primarily stem from varying crosslinking strategies utilized in these studies, however, there is a general lack of discussion on how the crosslinked strategies change the compressive strength in the existing literature. Moreover, the compressive stress of TCNF or TCNF/GO hydrogels sharply increased after being functionalized by PEI, increasing to 38.6 and 48.7 for

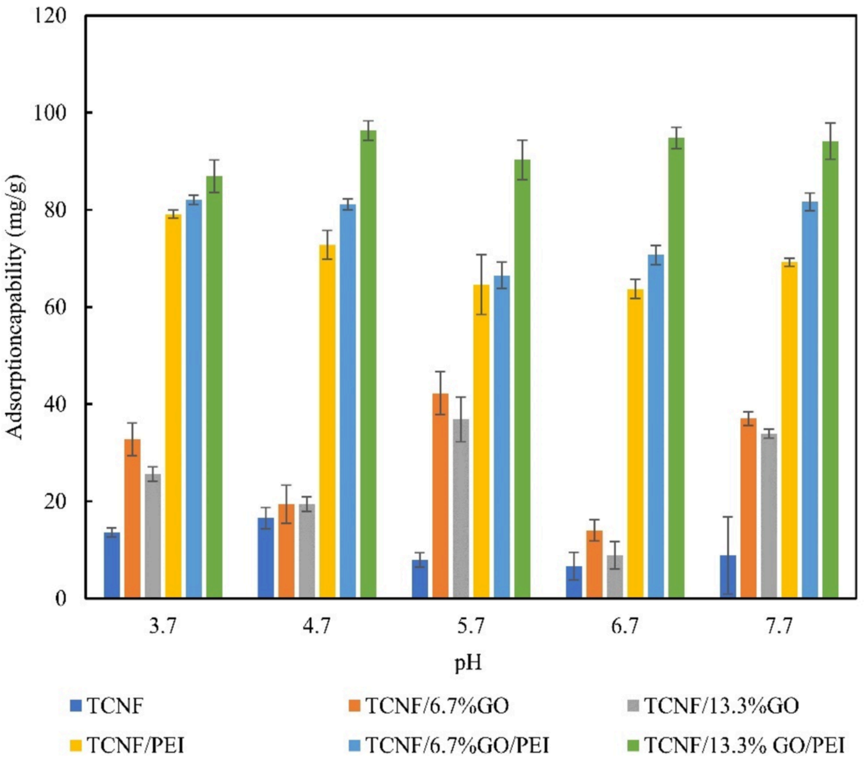

Fig. 6. The effect of GO and PEI modification on the adsorption capability of corresponding hydrogels.

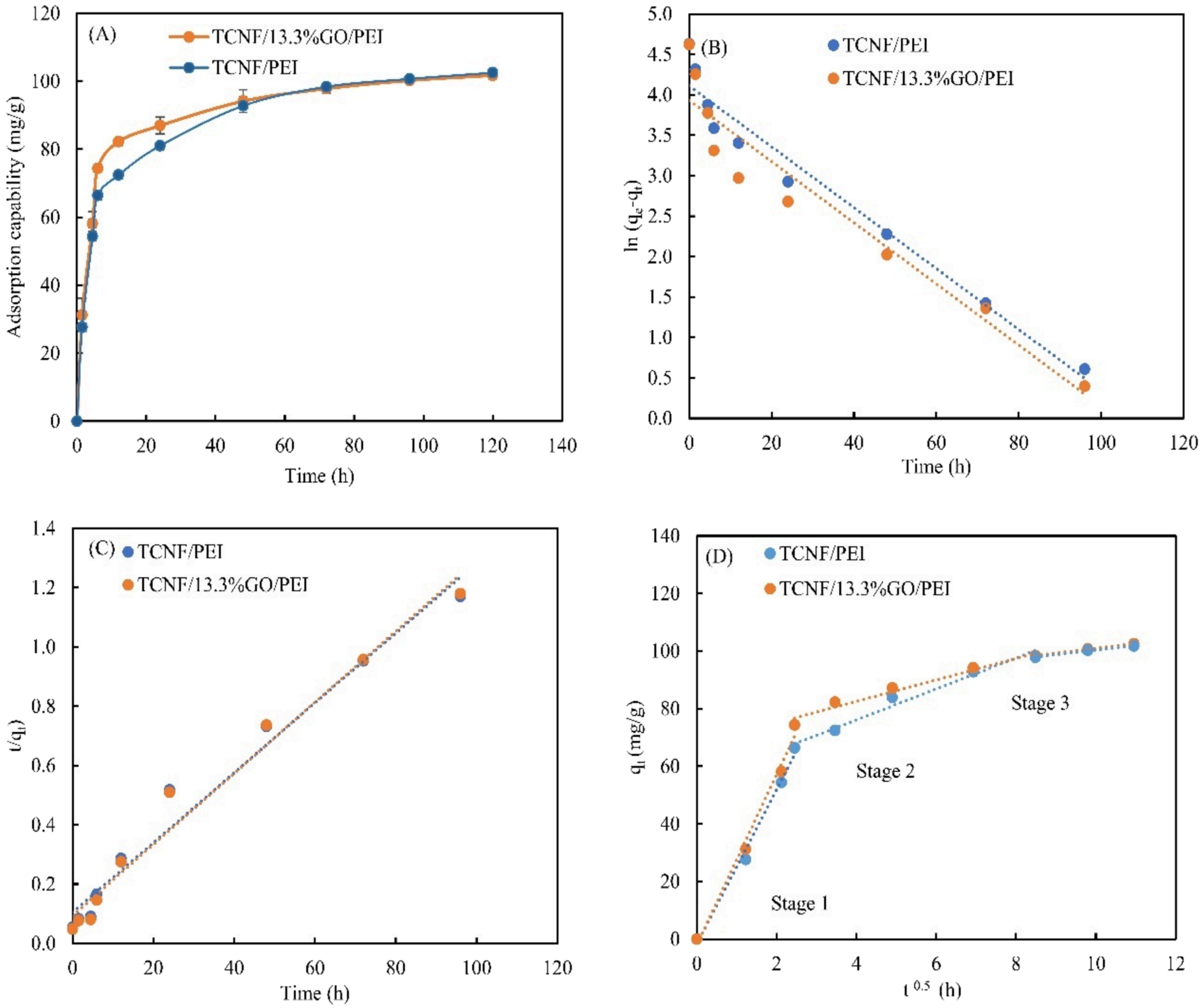

Fig. 7. The Pseudo- first order (A), Pseudo- second order (B) and Intra-particle diffusion model (C) for adsorption kinetics of TEMPO-CNF/PEI hydrogel and TEMPO-CNF/13.3 %GO/PEI hydrogel.

TCNF/PEI, and TCNF/6.7 %GO/PEI, hydrogels, respectively. This increase was mainly attributed to the abundant hydrogen bonding between PEI and TCNF or PEI and GO (Zhao et al., 2023). Subsequently, with further increases in the GO content, the compressive strength decreased, reaching 40.9 ± 5.8 for TCNF/13.3 %GO/PEI hydrogel. The trends in compression modulus and fracture strain followed a similar pattern to that of compressive stress. Therefore, the conclusion is that TCNF/6.7 %GO/PEI hydrogel show optimum strength and toughness.

3.3. Adsorption

3.3.1. Effect of GO addition

Testing was conducted to investigate the impact of GO addition on the adsorption performance of the corresponding hydrogel for methyl blue, an anionic dye. The adsorption process was examined within a pH range of 3.7–7.7 and measured after a 24 h period. As depicted in Fig. 6, the adsorption capacity of TCNF hydrogels increased after GO addition. In comparison to the TCNF hydrogel (7.9 mg/g), the adsorption capacity of the GO-modified CNF hydrogel showed an increase with higher GO content, reaching a maximum of 42.3 mg/g at a GO content of 6.7 % and a pH of 5.7. However, when the GO content continued to increase to 13.3 %, the adsorption capacity decreased to 36.9 mg/g. These results align with the changes observed in surface area and surface energy based on variations in GO content. Because of this improved behavior, further adsorption testing was conducted only with the 13.3 % GO containing hydrogels.

3.3.2. Effect of further PEI functionalization

Further modification of the TCNF and TCNF/GO hydrogels through physical adsorption of PEI led to a sharp increase in adsorption capacity. The adsorption capacity of TCNF/PEI hydrogel ranged from 64.6 to 79.1 mg/g within the pH range of 3.7–7.7 (Fig. 6). The adsorption capacity of TCNF/GO/PEI further increased with higher GO content, reaching 86.9–96.3 mg/g across the tested pH range. This increase can be attributed to the combined effect of surface area and surface energy. Although the surface energy decreased with increasing GO content for TCNF/GO/PEI hydrogel, the surface area increased. Consequently, GO-functionalized hydrogels exhibited lower adsorption capacity compared to PEI-functionalized ones due to the presence of electrostatic attraction between the PEI-modified hydrogel and methyl blue, as indicated by the higher total surface energy of the PEI-modified hydrogel mentioned earlier.

Furthermore, electrostatic attraction or repulsion, which depends primarily on pH, influenced the adsorption capacity when the GO content was below 13.3 % for both TCNF/GO and TCNF/GO/PEI hydrogels (Guo, An, Ran, Xiao, & Zhai, 2018; Yan et al., 2022). Conversely, the

Table 3
Parameters of Pseudo-first-order, Pseudo-second-order and Intra-particle diffusion model for adsorption kinetics.

Kinetic parameters	TCNF/PEI hydrogel	TCNF/13.3 % GO/PEI hydrogel
$q_{e, exp}$ (mg/g)	102.5	101.7
Pseudo-first order		
qe (mg/g)	60.9284	50.9885
K_1 (mg/(g*h))	−0.0377	−0.0378
R^2	0.9591	0.9211
Pseudo-second order		
qe (mg/g)	84.7458	84.7458
K_2 (mg/(g*h))	0.0013	0.0013
R^2	0.9745	0.9745
Intraparticle diffusion model		
$k_{i,1}$ (mg/(g*h))	26.9	29.6
c_1	−1.8	−1.9
R_1^2	0.9918	0.9890
$k_{i,2}$ (mg/(g*h))	5.4	3.7
c_2	54.6	67.7
R_2^2	0.9785	0.9637
$k_{i,3}$ (mg/(g*h))	1.7	1.6
c_3	84.2	84.5
R_3^2	0.9992	0.9902

adsorption capacity of TCNF/13.3 %GO/PEI hydrogel remained similar across all pH conditions. This suggests that when the GO content is below 13.3 %, the adsorption capacity is pH-dependent, whereas with a GO content of 13.3 %, the adsorption capacity becomes independent of pH. This finding indicates a different adsorption mechanism, prompting further investigation through adsorption kinetics and adsorption isotherm modeling to clarify this difference.

3.3.3. *Adsorption kinetics*

The adsorption capability and kinetics were evaluated using an initial concentration of 200 mg/L methyl blue with 0.0186 g of different types of hydrogels (Fig. 7 (A)). The results showed that the adsorption capability of TCNF/13.3%GO/PEI hydrogel reached 82.2 mg/g after just 12 h, while TCNF/PEI hydrogel needed 24 h to get to 85.9 mg/g. The time was cut in half for the TCNF/13.3%GO/PEI hydrogel to get almost the same adsorption capability as the TCNF/PEI hydrogel. However, the adsorption capability became similar after 48 h, up to 92.8 and 94.2 mg/g, respectively. This indicates that the addition of GO leads to an increase in the initial adsorption rate. This was further explored by adsorption kinetics modeling. The adsorption reached equilibrium after 120 h, with an adsorption capability of 102.5 mg/g and the adsorption efficiency was 96.8 %, which meant almost all methyl blue dyes were adsorbed at initial concentration of 200 mg/L.

The adsorption kinetics were modeled to learn more about the adsorption behavior. The data was fitted to pseudo-first-order and pseudo-second-order models (Fig. 7(B), (C) and Table 3). For both the TCNF/PEI and TCNF/13.3 % GO/PEI hydrogels, the R^2 of pseudo-second-order models were 0.9745 for both, which was higher than that of pseudo-first-order models (0.9591 and 0.9211). This meant that the adsorption kinetic model was more fitted to pseudo-second-order models. To further reveal the diffusion mechanism in the methyl blue dye adsorption process, the intra-particle diffusion model was tested. As shown in Fig. 7(D), the plots of q_t versus $t^{0.5}$ yielded three linear regions, which are assigned to three stages of diffusion of methyl blue dyes: (1) external diffusion from the bulk solution to the surface of the hydrogel, (2) internal diffusion from the surface to the inner section of the hydrogel once the surface sites are saturated, (3) slow diffusion until the surface became saturated (Tang et al., 2020). The slopes of the three stages were calculated from the intraparticle diffusion model and summarized in Table 2. It is evident that Kid,1 > Kid,2 > Kid,3, suggesting the adsorption rate in the first stage was faster than the other stages. This indicates the external surface adsorption process was faster than the intra-particle diffusion process. Compared with TCNF/PEI hydrogels (Kid,1 = 26.9; Kid,2 = 5.4; Kid,3 = 1.7), TCNF/13.3 % GO/PEI (Kid,1 = 29.6; Kid,2 = 3.7; Kid,3 = 1.6) has higher Kid,1 but lower Kid,2 and almost similar Kid,3. This was likely caused by the surface area increasing after adding 13.3 % of GO (TCNF/13.3 %GO/PEI) compared with without GO (TCNF/PEI). Nevertheless, the higher surface adsorption capability made the holes crowded according to SEM observation, so the diffusion rate from the surface to the inner section of the hydrogel

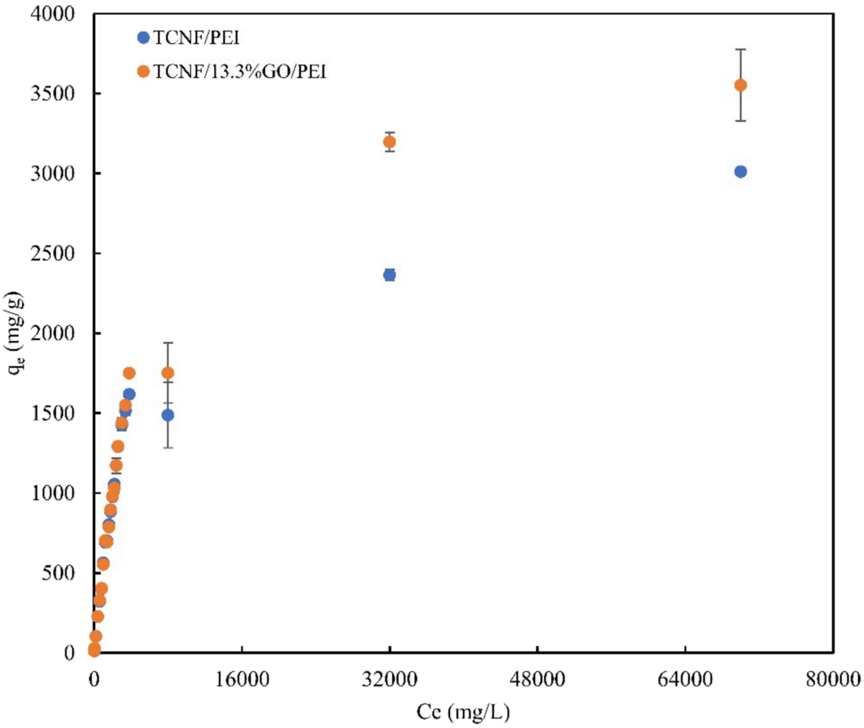

Fig. 8. The adsorption efficiency change of TEMPO-CNF/0.2GO/PEI hydrogel over time.

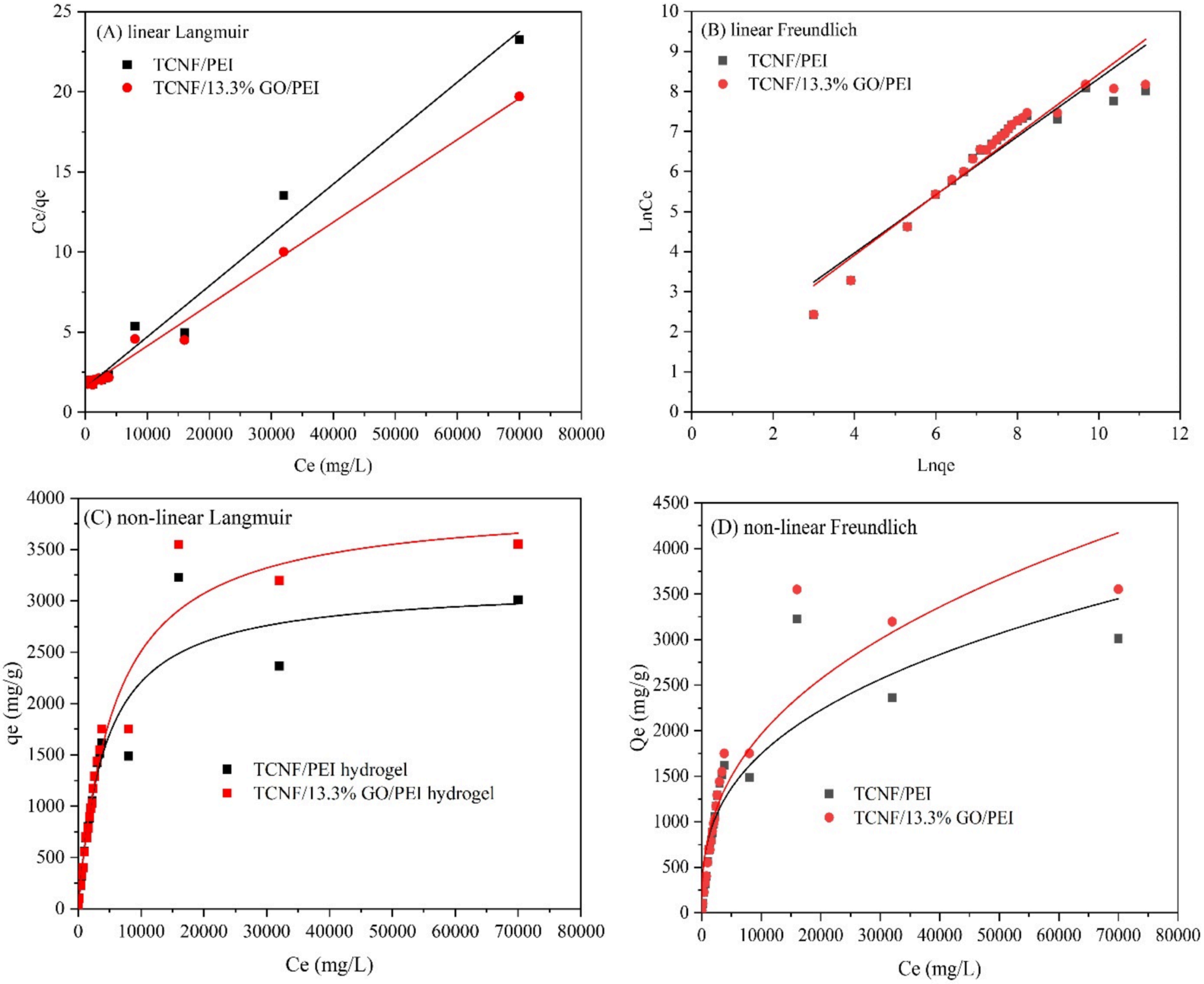

Fig. 9. Adsorption data fitted to linear and non-linear Langmuir and Freundlich isotherm model.

Table 4
Langmuir and Freundlich constants of TEMPO-CNF/PEI and TEMPO-CNF/13.3 % GO/PEI hydrogel for methyl blue adsorption.

Hydrogels	Adsorption isotherm		Equation	Model parameters	Statistics parameter
TCNF/PEI hydrogel	Linear model	Langmuir	$C_e/q_e = C_e/q_m + 1/(K_L{*}\ q_m)$	$q_m = 3125.0$ mg/g, $K_L = 0.00021$	$R^2 = 0.9829$
		Freundlich	$Lnq_e = LnK_F + (LnC_e)/n$	$K_F = 2.9084$, $n = 1.3789$	$R^2 = 0.8955$
	Non-linear model	Langmuir	$q_e = (q_m{*}K_L{*}\ C_e)/(1+K_L{*}\ C_e)$	$q_m = 3151.6$ mg/g, $K_L = 0.00023$	$R^2 = 0.9311$
		Freundlich	$q_e = (q_m{*}K_L{*}C_e)/(1+K_L{*}C_e)$	$K_F = 69.6226$, $n = 2.8586$	$R^2 = 0.8377$
TCNF/13.3 %GO/ PEI hydrogel	Linear model	Langmuir	$C_e/q_e = C_e/q_m + 1/(K_L{*}\ q_m)$	$q_m = 3846.2$ mg/g, $K_L = 0.00017$	$R^2 = 0.9914$
		Freundlich	$Lnq_e = LnK_F + (LnC_e)/n$	$K_F = 1.0937$, $n = 1.1141$	$R^2 = 0.9192$
	Non-linear model	Langmuir	$q_e = (q_m{*}K_L{*}\ C_e)/(1+K_L{*}\ C_e)$	$q_m = 3962.2$ mg/g, $K_L = 0.00017$	$R^2 = 0.9647$
		Freundlich	$q_e = (q_m{*}K_L{*}C_e)/(1+K_L{*}C_e)$	$K_F = 55.0140$, $n = 2.5773$	$R^2 = 0.8792$

became slower, likewise, the Kid,2 was lower. After those two stages, the adsorption almost reached adsorption equilibrium, and the adsorption capability changed slightly, leading to a similar Kid,3.

3.3.4. Adsorption isotherms

To obtain adsorption isotherms, dye concentrations were varied (Fig. 8). It was found that the adsorption capability of TCNF/PEI and TCNF/13.3 % GO/PEI hydrogel had the same trend at the beginning, in which the adsorption capability increased linearly with the increase of methyl blue concentration, reaching up to 1617 mg/g when methyl blue concentration was 3000 mg/L. Beyond that concentration, the adsorption capability increased slowly for both, with TCNF/13.3% GO/PEI hydrogels showing higher adsorption capability than TCNF/PEI, reaching up to 3551.8 and 3010.5 mg/g, respectively, at the maximum dye solubility (70 000 mg/L). This is due to the increase in the PEI content attached to the hydrogel and the resulting increase in surface area after the introduction of 13.3 % GO.

The adsorption data were fitted into the linear and non-linear Langmuir and Freundlich models to determine mechanisms and model maximum capacities (Fig. 9). The parameters obtained from the fittings are summarized in Table 4. Compared with the non-linear model, the correlation coefficient R^2 of linear Langmuir (0.9829, 0.9914; Fig. 9A) and Freundlich (0.8955, 0.9192; Fig. 9B) models were higher than that of the non-linear Langmuir model (0.9311, 0.9647; Fig. 9C) and Freundlich (0.8377, 0.8972; Fig. 9D) models for TCNF/PEI and TCNF/ 13.3 % GO/PEI hydrogels, respectively. The R^2 values of Langmuir

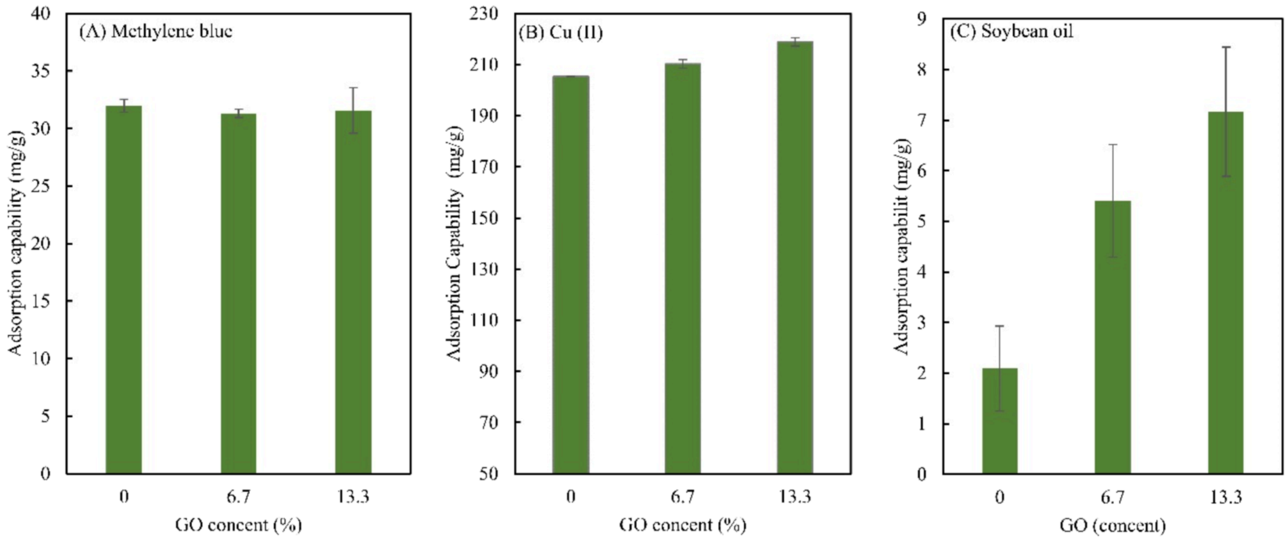

Fig. 10. Adsorption capability of TCNF/PEI and TCNF/13.3 % GO/PEI hydrogel for Methylene blue (+) dyes at initial concentration of 200 mg/L with pH 5.7 after 24 h (A), Cu (II) ions (B) and soybean oils (C), respectively.

Table 5
Compared with other materials.

Pollutants	Materials	Shape	Adsorption capability (mg/g)	References
Methyl blue (−)	Epoxy chloropropane and diethylenetriamine modified cellulose membrane prepared from corn stalk	Membrane	9.1	(Qiao et al., 2021)
	Carbon dots crosslinked chitosan/cellulose sponge	Sponge	297.6	(Lu, Yuan, Zhu, & Yu, 2021)
	Polyethyleneimine grafted starch nanocrystals	Powders	337.8	(Chen, Zhao, Xie, Liang, & Zong, 2021)
	Poly(methacrylic acid-*co*-2-(dimethylamino) ethyl methacrylate) and carboxylated cellulose nanofibrils	Aerogel	598.8	(Thomas et al., 2018)
	PEI-modified cellulose aerogels	Aerogel	1333.0	(Paladini et al., 2019)
	COOH-CNF/PEI	Hydrogel	**3125.0**	This work
	Polyaspartate−montmorillonite composite withquaternary phosphonium salt (Mt/IPS2)	Aerogel	7958.0	(Elsherbiny, El-Hefnawy, & Gemeay, 2017)
	Macroscopic yttrium oxide aerogel monoliths	Powder	8080.0	(Cheng, Rechberger, & Niederberger, 2016)
Methylene blue (+)	Wheat shells	Powder	16.6	(Bulut & Aydın, 2006)
	TCNF/GO/PEI	Hydrogel	**32.3**	This work
	Maleic anhydride modified cellulose	Powder	33.7	(Zhou, Jin, Hu, Zhang, & Ma, 2012)
	Cellulose-derived carbon/montmorillonite nanocomposites	Powder	138.1	(Tong et al., 2018)
	Carboxymethyl cellulose/carboxylated graphene oxide composite	Microbead	180.3	(Eltaweil, Elgarhy, El-Subruiti, & Omer, 2020)
	Sodium carboxymethyl cellulose (CMC) and carboxylated cellulose nanofibers	Aerogel	579.5	(Zhang, Xiao, Fan, He, & Qin, 2022)
	Calcium alginate hydrogels reinforced with cellulose nanocrystals	Hydrogel	676.7	(Soleimani, Heydari, Fattahi, & Motamedisade, 2023)
	Hemicellulose-based porous hydrogels	Hydrogels	1072.7	(Sun et al., 2015)
Cu (II)	TEMPO-mediated oxidized cellulose nanofibrils modified with PEI	Powder	53.0	(Zhang, Zang, Shi, Yu, & Sheng, 2016)
	Cellulose hydrogels	Hydrogel	119	(Santoso et al., 2022)
	Fluorescent carbon dots crosslinked cellulose Nanofibril/Chitosan	Hydrogel	148.3	(Chen et al., 2022)
	TCNF/GO/PEI HYDROGEL	Hydrogel	**218.5**	This work
	Cellulose nanofiber/polyacrylamide aerogel	Aerogel	240.0	(Mo, Zhang, Qi, & Huang, 2022)
	Modified carboxymethyl cellulose hydrogel adsorbent	Hydrogel	260.7	(Sun et al., 2022)
	Carbon/Carborundum@Microcrystalline Cellulose core shell nanocomposite	Powder	423.6	(Mubarak, Zayed, & Ahmed, 2022)
	Nanocellulose-based polyethylenimine aerogels	Aerogel	485.4	(Mo, Pang, Tan, Zhang, & Li, 2019)
	Amio-functionalized cellulose composite	Aerogel	562.2	(Qin et al., 2024)
Soybean oils	TCNF/GO/PEI	Hydrogel	**7200**	This work
	Hybrid carbon aerogels	Aerogel	10,000	(Phat et al., 2022)
	Porous polycarbonate/carboxyl-functionalized multiwalled carbon nanotubes	Aerogel	12,600	(Li et al., 2018)
	Graphene–poly(vinyl alcohol) composites	Powder	48,700	(Wang, Chang, Zheng, & Ma, 2014)

models were higher than those of Freundlich models, suggesting that the homogenous monolayer adsorption was predominant (Guo, An, Xiao, Zhai, & Shi, 2017). The adsorption isotherm model agreed with the cellulose-PEI aerogel crosslinked by glutaraldehyde (Guo et al., 2018). These similar results confirmed that the availability of amino groups was the determinant factor in the adsorption mechanism rather than the crosslinking process utilized.

Based on the above, linear Langmuir is the best to describe the adsorption behavior. The maximum adsorption capability predicted by the linear Langmuir model for TCNF/PEI and TCNF/13.3 % GO/PEI hydrogels were 3125.0 and 3846.2 mg/g, respectively. Confirming that adding GO can increase the maximum adsorption capability.

3.3.5. Adsorption for various pollutants

The adsorption capability for methylene blue (+), Cu (II) and soybean oil were tested to access the potential of transferring those materials for various species of water pollutants. Compared with TCNF/PEI hydrogel, the adsorption capability of TCNF/13.3 %GO/PEI hydrogel for methylene blue (+) dyes did not change (32.3 mg/g) (Fig. 10A). This result could be expected as the main driving mechanism for the toxic dyes adsorption is electrostatic attractive interaction (Qiao et al., 2021). However, it is possible that negatively charged carboxyl groups present on GO were occluded by the positively charged PEI, resulting in dampening electrostatic attractive interaction between the hydrogel surface and methylene blue dyes. Additionally, the result indicated that the differences in surface area and surface energy upon GO addition were not significant enough to cause a difference for methylene blue adsorption. However, the adsorption capability for Cu (II) ions and soybean oil increased from 205.3 to 218.5 and 2.1 to 7.2 mg/g, respectively (Fig. 10B and C). The increase in copper ion capturing is most likely due to the introduction of more oxygen containing groups in the hydrogels with higher GO content, which helps coordinate with the ions (Yap et al., 2021). Conversely, soybean oil capturing would be driven by the interaction with the hydrophobic faces of the reduced graphene oxide (rGO), which are formed from GO after PEI reducing. Compared with other materials that have been reported, the adsorption capability of TCNF/GO/PEI hydrogel for methylene blue (+) dyes and soybean oils is relatively lower, while adsorption capability for methyl blue (−) dyes and Cu (II) was higher than most of other materials (Table 5). These results confirmed that TCNF/GO/PEI hydrogel has great potential for the removal of multiple pollutants from water resources.

3.4. Regeneration of TCNF/PEI hydrogel

The biosorption process is only economically viable if the biosorbent is reused and recycled after desorption of contaminants (Reshmy et al., 2022). Usually, the desorption method is decided by the adsorption mechanism. Here, the adsorption mechanism is mainly driven by electrostatic interaction, so the dyes can be desorbed from the adsorbent by drastically changing the pH of the solution, based on previous research. A solution of sodium hydroxide (1 M) was used for the desorption of dyes. After 4 cycles, the adsorption efficiency of TCNF/13.3 %GO/PEI hydrogel remained higher than 77 %, indicating that the hydrogels have the capability of being recycled multiple times (Fig. S1).

4. Conclusion

A facile and cost-effective self-assembling route was developed for preparing TCNF/GO/PEI composite hydrogels. Initially, TCNF/GO was chelated by cationic ions into TCNF/GO hydrogel, which was subsequently functionalized by PEI with physical adsorption to obtain the final TCNF/GO/PEI hydrogel. Compared with TCNF hydrogel, the surface area, surface energy, and adsorption capability of TCNF/GO hydrogels showed improvement at an optimum loading of GO content of 6.7 %, mainly benefiting from the high surface area and the multiple functional groups present in GO. After further amine-functionalization of the TCNF/GO hydrogels using PEI, surface energy, mechanical strength, and adsorption capability were significantly increased, which was attributed to an increase of the overall available amine active sites that resulted in strong hydrogen bonding. However, beyond the GO content of 13.3 %, these properties were negatively impacted due to the aggregation of adjacent GO sheets in high GO content. Furthermore, the addition of GO to the hydrogels did not impact the adsorption mechanisms but increased the external diffusion rates as evidenced by the models demonstrated in this work. The adsorption capability of optimized TCNF/GO/PEI hydrogel was overall improved for methyl blue anionic dyes, Cu (II), and soybean oil, mainly attributed to electrostatic, chelation and hydrophobic effects, respectively. In the case of methyl blue adsorption, the maximum adsorption capability increased by 22 % at the maximum GO loading at the maximum dye solubility. These findings highlight the significant potential of TCNF/GO/PEI hydrogels for the efficient removal of various pollutants from water. Given the complex nature of real-world water contamination, future research should focus on optimizing hydrogels for systems containing multiple contaminants to better address diverse environmental challenges. However, the disposal of TCNF/GO/PEI hydrogel after adsorption a variety of pollutants should be considered. Likewise, a more in-depth study of the reuse of the composite hydrogel needs to be done to determine the impacts and capacity.

Ethics approval and consent to participate

Not applicable.

Consent for publication

Not applicable.

Funding

This work was supported by the National Science Foundation CAREER award (2119809) through the BMAT program in the Division of Materials Research and the EPSCoR program. Likewise, the USDA National Institute of Food and Agriculture, Hatch program (ALA013-17003), and McIntire-Stennis program (1022526) are acknowledged for the support of this work. The authors also want to acknowledge the support from Chinese Scholarship Council (201906300036).

CRediT authorship contribution statement

Yufei Nan: Writing – original draft, Visualization, Project administration, Methodology, Formal analysis, Data curation, Conceptualization. **Diego Gomez-Maldonado:** Writing – review & editing, Visualization, Methodology, Formal analysis, Conceptualization. **Kailong Zhang:** Writing – review & editing, Methodology, Data curation. **Haishun Du:** Writing – review & editing, Methodology, Formal analysis. **Daniel C. Whitehead:** Writing – review & editing, Methodology. **Mi Li:** Writing – review & editing, Methodology. **Xinyu Zhang:** Writing – review & editing, Methodology. **Maria Soledad Peresin:** Writing – review & editing, Visualization, Methodology, Formal analysis, Conceptualization.

Declaration of competing interest

The authors declare that they have no known competing financial interests or personal relationships that could have appeared to influence the work reported in this paper.

Data availability

Data is available upon reasonable request to authors.

Acknowledgments

Not applicable.

Supplementary materials

Supplementary material associated with this article can be found, in the online version, at doi:10.1016/j.carpta.2024.100585.

References

Aliyari, E., Alvand, M., & Shemirani, F. (2016). Modified surface-active ionic liquid-coated magnetic graphene oxide as a new magnetic solid phase extraction sorbent for preconcentration of trace nickel. *RSC Advances, 6*(69), 64193–64202. https://doi.org/10.1039/C6RA04163A

Bai, W., Yu, H., Liu, L., Pakdel, E., Tang, B., Su, H., et al. (2023). The adsorption kinetics and mechanism of odorous gases onto textile fibers. *RSC Sustainability, 1*(2), 357–367. https://doi.org/10.1039/D2SU00086E

Bulut, Y., & Aydın, H. (2006). A kinetics and thermodynamics study of methylene blue adsorption on wheat shells. *Desalination, 194*(1–3), 259–267. https://doi.org/10.1016/j.desal.2005.10.032

Chaiyakun, S., Witit-Anun, N., Nuntawong, N., Chindaudom, P., Oaew, S., Kedkeaw, C., et al. (2012). Preparation and characterization of graphene oxide nanosheets. *Procedia Engineering, 32*, 759–764. https://doi.org/10.1016/j.proeng.2012.02.009

Chatterjee, S., Ke, W.-T., & Liao, Y.-C. (2020). Elastic nanocellulose/graphene aerogel with excellent shape retention and oil absorption selectivity. *Journal of the Taiwan Institute of Chemical Engineers, 111*, 261–269. https://doi.org/10.1016/j.jtice.2020.04.020

Chen, J., Yao, B., Li, C., & Shi, G. (2013). An improved hummers method for eco-friendly synthesis of graphene oxide. *Carbon, 64*, 225–229. https://doi.org/10.1016/j.carbon.2013.07.055

Chen, Q., Zhao, Y., Xie, Q., Liang, C., & Zong, Z. (2021). Polyethyleneimine grafted starch nanocrystals as a novel biosorbent for efficient removal of methyl blue dye. *Carbohydrate Polymers, 273*, Article 118579. https://doi.org/10.1016/j.carbpol.2021.118579

Chen, X., Song, Z., Yuan, B., Li, X., Li, S., Nguyen, T. T., et al. (2022). Fluorescent carbon dots crosslinked cellulose Nanofibril/Chitosan interpenetrating hydrogel system for sensitive detection and efficient adsorption of Cu (II) and Cr (VI). *Chemical Engineering Journal, 430*, Article 133154. https://doi.org/10.1016/j.cej.2021.133154

Cheng, W., Rechberger, F., & Niederberger, M. (2016). Three-dimensional assembly of yttrium oxide nanosheets into luminescent aerogel monoliths with outstanding adsorption properties. *ACS Nano, 10*(2), 2467–2475. https://doi.org/10.1021/acsnano.5b07301

Ding, P., Su, S., Song, N., Tang, S., Liu, Y., & Shi, L. (2014). Influence on thermal conductivity of polyamide-6 covalently-grafted graphene nanocomposites: Varied grafting-structures by controllable macromolecular length. *RSC Advances, 4*(36), 18782–18791. https://doi.org/10.1039/C4RA00500G

Dong, H., Snyder, J. F., Williams, K. S., & Andzelm, J. W. B. (2013). Cation-induced hydrogels of cellulose nanofibrils with tunable moduli. *Biomacromolecules, 14*(9), 3338–3345. https://doi.org/10.1021/bm400993f

Elsherbiny, A. S., El-Hefnawy, M. E., & Gemeay, A. H. (2017). Linker impact on the adsorption capacity of polyaspartate/montmorillonite composites towards methyl blue removal. *Chemical Engineering Journal, 315*, 142–151. https://doi.org/10.1016/j.cej.2017.01.002

Eltaweil, A. S., Elgarhy, G. S., El-Subruiti, G. M., & Omer, A. M. (2020). Carboxymethyl cellulose/carboxylated graphene oxide composite microbeads for efficient adsorption of cationic methylene blue dye. *International Journal of Biological Macromolecules, 154*, 307–318. https://doi.org/10.1016/j.ijbiomac.2020.03.122

Escher, B. I., Stapleton, H. M., & Schymanski, E. L. (2020). Tracking complex mixtures of chemicals in our changing environment. *Science, 367*(6476), 388–392. https://doi.org/10.1126/science.aay6636

Fang, Y. Y., He, H., Dong, K. Q., Yang, J. S., & Qin, Z. Y. (2022). Preparation and adsorption properties of hyperbranched polyethyleneimine-cellulose nanofiber aerogel. *New Journal of Chemistry, 46*(13), 5954–5965. https://doi.org/10.1039/D1NJ06156A

Geng, J., Yin, Y., Liang, Q., Zhu, Z., & Luo, H. (2019). Polyethyleneimine cross-linked graphene oxide for removing hazardous hexavalent chromium: Adsorption performance and mechanism. *Chemical Engineering Journal, 361*, 1497–1510. https://doi.org/10.1016/j.cej.2018.10.141

Ghasemlou, M., Daver, F., Ivanova, E. P., Habibi, Y., & Adhikari, B. (2021). Surface modifications of nanocellulose: From synthesis to high-performance nanocomposites. *Progress in Polymer Science, 119*, Article 101418. https://doi.org/10.1016/j.progpolymsci.2021.101418

Guo, D.-M., An, Q.-D., Xiao, Z.-Y., Zhai, S.-R., & Shi, Z. (2017). Polyethylenimine-functionalized cellulose aerogel beads for efficient dynamic removal of chromium (VI) from aqueous solution. *RSC Advances, 7*(85), 54039–54052. https://doi.org/10.1039/C7RA09940A

Guo, D. M., An, Q. D., Ran, L., Xiao, Z. Y., & Zhai, S. R. (2018). Ultrahigh selective and efficient removal of anionic dyes by recyclable polyethylenimine-modified cellulose aerogels in batch and fixed-bed systems. *Colloids and Surfaces A, 555*, 150–160. https://doi.org/10.1016/j.colsurfa.2018.06.081

He, H., Cheng, M. X., Liang, Y. T., Zhu, H. X., Sun, Y. P., Dong, D., et al. (2020). Intelligent cellulose nanofibers with excellent biocompatibility enable sustained antibacterial and drug release via a pH-responsive mechanism. *Journal of Agricultural and Food Chemistry, 68*(11), 3518–3527. https://doi.org/10.1021/acs.jafc.9b06588

Hernandez, J. A., Soni, B., Iglesias, M. C., Vega Erramuspe, I. B., Frazier, C. E., & Peresin, M. S. (2022). Soybean hull pectin and nanocellulose: Tack properties in aqueous pMDI dispersions. *Journal of Materials Science, 57*(8), 5022–5035. https://doi.org/10.1007/s10853-022-06938-x

Hlongwane, G. N., Sekoai, P. T., Meyyappan, M., & Moothi, K. (2019). Simultaneous removal of pollutants from water using nanoparticles: A shift from single pollutant control to multiple pollutant control. *Science of the Total Environment, 656*, 808–833. https://doi.org/10.1016/j.scitotenv.2018.11.257

Hou, C., Zhang, Q., Li, Y., & Wang, H. (2012). P25—Graphene hydrogels: Room-temperature synthesis and application for removal of methylene blue from aqueous solution. *Journal of Hazardous Materials, 205*, 229–235. https://doi.org/10.1016/j.jhazmat.2011.12.071

Hwang, Y. N., Kim, H., Lee, Y., & Park, S.-C. (2023). Evolution of the surface energy of BaTiO$_3$ nanoparticles in the course of dispersant coating; An inverse gas chromatography study. *Colloids and Surfaces A: Physicochemical and Engineering Aspects.* , Article 131888. https://doi.org/10.1016/j.colsurfa.2023.131888

Jiang, F., Zhao, W., Wu, Y., Wu, Y., Liu, G., Dong, J., et al. (2019). A polyethyleneimine-grafted graphene oxide hybrid nanomaterial: Synthesis and anti-corrosion applications. *Applied Surface Science, 479*, 963–973. https://doi.org/10.1016/j.apsusc.2019.02.193

Kim, Y., Bang, J., Kim, J., Choi, J. H., Hwang, S. W., Yeo, H., & Kwak, H. W. (2022). Cationic surface-modified regenerated nanocellulose hydrogel for efficient Cr(VI) remediation. *Carbohydrate Polymers, 278*, Article 118930. https://doi.org/10.1016/j.carbpol.2021.118930

Köklükaya, O., Carosio, F., & Wågberg, L. (2018). Tailoring flame-retardancy and strength of papers via layer-by-layer treatment of cellulose fibers. *Cellulose, 25*(4), 2691–2709. https://doi.org/10.1007/s10570-018-1749-8

Landrigan, P. J., Stegeman, J. J., Fleming, L. E., Allemand, D., Anderson, D. M., Backer, L. C., et al. (2020). Human health and ocean pollution. *Annals of Global Health, 86*(1), 151. https://doi.org/10.5334/aogh.2831

Li, N., Zhang, H., Xiao, Y., Huang, Y. S., Xu, M. D., You, D. L., et al. (2019). Fabrication of cellulose-nanocrystal-based folate targeted nanomedicine via layer-by-layer assembly with lysosomal pH-controlled drug release into the nucleus. *Biomacromolecules, 20*(2), 937–948. https://doi.org/10.1021/acs.biomac.8b01556

Li, Y. Q., Gong, Q., Han, L., Liu, X. H., Yang, Y., Chen, C., et al. (2022). Carboxymethyl cellulose assisted polyaniline in conductive hydrogels for high-performance self-powered strain sensors. *Carbohydrate Polymers, 298*, Article 120060. https://doi.org/10.1016/j.carbpol.2022.120060

Li, Z., Wang, B., Qin, X., Wang, Y., Liu, C., Shao, Q., et al. (2018). Superhydrophobic/superoleophilic polycarbonate/carbon nanotubes porous monolith for selective oil adsorption from water. *ACS Sustainable Chemistry and Engineering, 6*(11), 13747–13755. https://doi.org/10.1021/acssuschemeng.8b01637

Liu, J., Huang, Y., Zhang, G., Wang, Q., Shen, S., Liu, D., et al. (2024). Dialdehyde cellulose (DAC) and polyethyleneimine (PEI) coated polyvinylidene fluoride (PVDF) membrane for simultaneously removing emulsified oils and anionic dyes. *Journal of Hazardous Materials, 471*, Article 134341. https://doi.org/10.1016/j.jhazmat.2024.134341

Liang, L., Bhagia, S., Li, M., Huang, C., & Ragauskas, A. J. (2020). Cross-linked nanocellulosic materials and their applications. *Chemsuschem, 13*(1), 78–87. https://doi.org/10.1002/cssc.201901676

Liu, C., Jin, R. N., Ouyang, X. K., & Wang, Y. G. (2017). Adsorption behavior of carboxylated cellulose nanocrystal-polyethyleneimine composite for removal of Cr (VI) ions. *Applied Surface Science, 408*, 77–87. https://doi.org/10.1016/j.apsusc.2017.02.265

Liu, H., Guo, J., Zhou, Y., & Qian, J. (2020). Preparation and adsorption performance of efficient adsorbent for heavy metal copper (II) using graphene-oxide-based composites. *ChemistrySelect, 5*(36), 11354–11360. https://doi.org/10.1002/slct.202003189

Liu, Y. Y., Fan, Q., Huo, Y., Li, M., Liu, H. B., & Li, B. (2021). Construction of nanocellulose-based composite hydrogel with a double packing structure as an intelligent drug carrier. *Cellulose, 28*(11), 6953–6966. https://doi.org/10.1007/s10570-021-03978-5

Lu, P., Yang, Y., Liu, R., Liu, X., Ma, J., Wu, M., et al. (2020). Preparation of sugarcane bagasse nanocellulose hydrogel as a colourimetric freshness indicator for intelligent food packaging. *Carbohydrate Polymers, 249*, Article 116831. https://doi.org/10.1016/j.carbpol.2020.116831

Lu, S., Yuan, G., Zhu, Y., & Yu, S. (2021). Carbon dots crosslinked chitosan/cellulose sponge capture of methyl blue by an adsorption process. *Luminescence, 36*(6), 1459–1468. https://doi.org/10.1002/bio.4089

Makhado, E., Pandey, S., Modibane, K. D., Kang, M., & Hato, M. J. (2020). Sequestration of methylene blue dye using sodium alginate poly (acrylic acid)@ ZnO hydrogel nanocomposite: Kinetic, isotherm, and thermodynamic investigations. *International Journal of Biological Macromolecules, 162*, 60–73. https://doi.org/10.1016/j.ijbiomac.2020.06.143

Mariano, M., Pilate, F., de Oliveira, F. B., Khelifa, F., Dubois, P., Raquez, J.-M., et al. (2017). Preparation of cellulose nanocrystal-reinforced poly (lactic acid) nanocomposites through noncovalent modification with PLLA-based surfactants. *ACS Omega, 2*(6), 2678–2688. https://doi.org/10.1021/acsomega.7b00387

Mo, L., Pang, H., Tan, Y., Zhang, S., & Li, J. (2019). 3D multi-wall perforated nanocellulose-based polyethylenimine aerogels for ultrahigh efficient and reversible removal of Cu (II) ions from water. *Chemical Engineering Journal, 378*, Article 122157. https://doi.org/10.1016/j.cej.2019.122157

Mo, L., Zhang, S., Qi, F., & Huang, A. (2022). Highly stable cellulose nanofiber/polyacrylamide aerogel via in-situ physical/chemical double crosslinking for highly efficient Cu (II) ions removal. *International Journal of Biological Macromolecules, 209*, 1922–1932. https://doi.org/10.1016/j.ijbiomac.2022.04.167

Mondal, J., & Srivastava, S. K. (2020). δ-MnO$_2$ nanoflowers and their reduced graphene oxide nanocomposites for electromagnetic interference shielding. *ACS Applied Nano Materials, 3*(11), 11048–11059. https://doi.org/10.1021/acsanm.0c02247

Mubarak, M. F., Zayed, A. M., & Ahmed, H. A. (2022). Activated carbon/carborundum@ microcrystalline cellulose core shell nano-composite: Synthesis, characterization and application for heavy metals adsorption from aqueous solutions. *Industrial Crops and Products, 182*, Article 114896. https://doi.org/10.1016/j.indcrop.2022.114896

Nan, Y., Gomez-Maldonado, D., Iglesias, M. C., Whitehead, D. C., & Peresin, M. S. (2023b). Valorized soybean hulls as TEMPO-oxidized cellulose nanofibril and polyethylenimine composite hydrogels and their potential removal of water pollutants. *Cellulose, 30*(6), 3639–3651. https://doi.org/10.1007/s10570-023-05086-y

Nan, Y., Gomez-Maldonado, D., Whitehead, D., Yang, M., & Peresin, M. S. (2023a). Comparison between nanocellulose-polyethyleneimine composites synthesis methods towards multiple water pollutants removal: A review. *International Journal of Biological Macromolecules, 232*, Article 123342. https://doi.org/10.1016/j.ijbiomac.2023.123342

Nguyen, V. T., Ha, L. Q., Nguyen, T. D., Ly, P. H., Nguyen, D. M., & Hoang, D. (2021). Nanocellulose and graphene oxide aerogels for adsorption and removal methylene blue from an aqueous environment. *ACS Omega, 7*(1), 1003–1013. https://doi.org/10.1021/acsomega.1c05586

Nikkhah, S., Tahermansouri, H., & Chekin, F. (2018). Synthesis, characterization, and electrochemical properties of the modified graphene oxide with 4, 4′-methylenedianiline. *Materials Letters, 211*, 323–327. https://doi.org/10.1016/j.matlet.2017.10.037

Ono, Y., Takeuchi, M., Zhou, Y., & Isogai, A. (2021). TEMPO/NaBr/NaClO and NaBr/NaClO oxidations of cotton linters and ramie cellulose samples. *Cellulose, 28*(10), 6035–6049. https://doi.org/10.1007/s10570-021-03944-1

Pal, A., Kondor, A., Mitra, S., Thu, K., Harish, S., & Saha, B. B. (2019). On surface energy and acid–base properties of highly porous parent and surface treated activated carbons using inverse gas chromatography. *Journal of Industrial and Engineering Chemistry, 69*, 432–443. https://doi.org/10.1016/j.jiec.2018.09.046

Paladini, G., Venuti, V., Almásy, L., Melone, L., Crupi, V., Majolino, D., et al. (2019). Cross-linked cellulose nano-sponges: A small angle neutron scattering (SANS) study. *Cellulose, 26*, 9005–9019. https://doi.org/10.1007/s10570-019-02732-2

Pang, Y., Zeng, G., Tang, L., Zhang, Y., Liu, Y., Lei, X., et al. (2011). PEI-grafted magnetic porous powder for highly effective adsorption of heavy metal ions. *Desalination, 281*, 278–284. https://doi.org/10.1016/j.desal.2011.08.001

Papavlu, A. P., Dinca, V., Filipescu, M., & Dinescu, M. (2017). Matrix-assisted pulsed laser evaporation of organic thin gilms: Applications in biology and chemical sensors. In T. E Itina (Ed.), *Laser ablation—From fundamentals to applications* (pp. 171–189). Rijeka, Croatia: InTech. https://doi.org/10.5772/intechopen.70676.

Phat, L. N., Tram, T. D. T., Lam, H. D. N., Khoa, B. D. D., Nguyen, H. C., Trung, N. K., et al. (2022). Synthesis of hybrid carbon aerogels from sugarcane bagasse and coffee grounds for oil adsorption application. *Biomass Conversion and Biorefinery*, 1–15. https://doi.org/10.1007/s13399-022-02924-0

Qiao, A., Cui, M., Huang, R., Ding, G., Qi, W., He, Z., et al. (2021). Advances in nanocellulose-based materials as adsorbents of heavy metals and dyes. *Carbohydrate Polymers, 272*, Article 118471. https://doi.org/10.1016/j.carbpol.2021.118471

Qin, Y., Chai, B., Sun, Y., Zhang, X., Fan, G., & Song, G. (2024). Amino-functionalized cellulose composite for efficient simultaneous adsorption of tetracycline and copper ions: Performance, mechanism and DFT study. *Carbohydrate Polymers, 332*, Article 121935. https://doi.org/10.1016/j.carbpol.2024.121935

Qiu, X., Wang, X., & Chen, S. (2022). A stable and easily regenerable solid amine adsorbent derived from a polyethylenimine-impregnated dialdehyde-cellulose/graphene-oxide composite. *New Journal of Chemistry, 46*(15), 6956–6965. https://doi.org/10.1039/D2NJ00530A

Reshmy, R., Philip, E., Madhavan, A., Pugazhendhi, A., Sindhu, R., Sirohi, R., et al. (2022). Nanocellulose as green material for remediation of hazardous heavy metal contaminants. *Journal of Hazardous Materials, 424*, Article 127516. https://doi.org/10.1016/j.jhazmat.2021.127516

Riva, L., Fiorati, A., & Punta, C. (2021). Synthesis and application of cellulose-polyethyleneimine composites and nanocomposites: A concise review. *Materials (Basel), 14*(3), 473. https://doi.org/10.3390/ma14030473

Riva, L., Lotito, A. D., Punta, C., & Sacchetti, A. (2022a). Zinc- and copper-loaded nanosponges from cellulose nanofibers hydrogels: New heterogeneous catalysts for the synthesis of aromatic acetals. *Gels, 8*(1), 54. https://doi.org/10.3390/gels8010054

Riva, L., Nicastro, G., Liu, M. C., Battocchio, C., Punta, C., & Sacchetti, A. (2022b). Pd-loaded cellulose NanoSponge as a heterogeneous catalyst for Suzuki–Miyaura coupling reactions. *Gels, 8*(12), 789. https://doi.org/10.3390/gels8120789

Riva, L., Punta, C., & Sacchetti, A. (2020). Co-polymeric nanosponges from cellulose biomass as heterogeneous catalysts for amine-catalyzed organic reactions. *Chemcatchem, 12*(24), 6214–6222. https://doi.org/10.1002/cctc.202001157

Ruiz, S., Tamayo, J. A., Delgado Ospina, J., Navia Porras, D. P., Valencia Zapata, M. E., Mina Hernandez, J. H., et al. (2019). Antimicrobial films based on nanocomposites of chitosan/poly (vinyl alcohol)/graphene oxide for biomedical applications. *Biomolecules, 9*(3), 109. https://doi.org/10.3390/biom9030109

Santoso, S. P., Angkawijaya, A. E., Bundjaja, V., Kurniawan, A., Yuliana, M., Hsieh, C.-W., et al. (2022). Investigation of the influence of crosslinking activation methods on the physicochemical and Cu (II) adsorption characteristics of cellulose hydrogels. *Journal of Environmental Chemical Engineering, 10*(1), Article 106971. https://doi.org/10.1016/j.jece.2021.106971

Sharma, N., Sharma, V., Jain, Y., Kumari, M., Gupta, R., Sharma, S., et al. (2017). Synthesis and characterization of graphene oxide (GO) and reduced graphene oxide (rGO) for gas sensing application. *Macromolecular Symposia, 376*, Article 1700006. https://doi.org/10.1002/masy.201700006. Wiley Online Library.

Soleimani, S., Heydari, A., Fattahi, M., & Motamedisade, A. (2023). Calcium alginate hydrogels reinforced with cellulose nanocrystals for methylene blue adsorption: Synthesis, characterization, and modelling. *Industrial Crops and Products, 192*, Article 115999. https://doi.org/10.1016/j.indcrop.2022.115999

Strokal, M., Spanier, J. E., Kroeze, C., Koelmans, A. A., Flörke, M., Franssen, W., et al. (2019). Global multi-pollutant modelling of water quality: Scientific challenges and future directions. *Current Opinion in Environmental Sustainability, 36*, 116–125. https://doi.org/10.1016/j.cosust.2018.11.004

Sun, X. F., Gan, Z., Jing, Z., Wang, H., Wang, D., & Jin, Y. (2015). Adsorption of methylene blue on hemicellulose-based stimuli-responsive porous hydrogel. *Journal of Applied Polymer Science, 132*(10), 41606. https://doi.org/10.1002/app.41606

Sun, Z., Yin, Y., An, Y., Deng, C., Wei, Z., Jiang, Z., et al. (2022). A novel modified carboxymethyl cellulose hydrogel adsorbent for efficient removal of poisonous metals from wastewater: Performance and mechanism. *Journal of Environmental Chemical Engineering, 10*(4), Article 108179. https://doi.org/10.1016/j.jece.2022.108179

Tang, C., Brodie, P., Li, Y., Grishkewich, N. J., Brunsting, M., & Tam, K. C. (2020). Shape recoverable and mechanically robust cellulose aerogel beads for efficient removal of copper ions. *Chemical Engineering Journal, 392*, Article 124821. https://doi.org/10.1016/j.cej.2020.124821

Tardy, B. L., Yokota, S., Ago, M., Xiang, W., Kondo, T., Bordes, R., et al. (2017). Nanocellulose–surfactant interactions. *Current Opinion in Colloid and Interface Science, 29*, 57–67. https://doi.org/10.1016/j.cocis.2017.02.004

Thomas, B., Raj, M. C., Joy, J., Moores, A., Drisko, G. L., & Sanchez, C. (2018). Nanocellulose, a versatile green platform: From biosources to materials and their applications. *Chemical Reviews, 118*(24), 11575–11625. https://doi.org/10.1021/acs.chemrev.7b00627

Thoniyot, P., Tan, M. J., Karim, A. A., Young, D. J., & Loh, X. J. (2015). Nanoparticle–hydrogel composites: Concept, design, and applications of these promising, multi-functional materials. *Advanced Science, 2*(1-2), Article 1400010. https://doi.org/10.1002/advs.201400010

Tong, D. S., Wu, C. W., Adebajo, M. O., Jin, G. C., Yu, W. H., Ji, S. F., et al. (2018). Adsorption of methylene blue from aqueous solution onto porous cellulose-derived carbon/montmorillonite nanocomposites. *Applied Clay Science, 161*, 256–264. https://doi.org/10.1016/j.clay.2018.02.017

Wang, N., Chang, P. R., Zheng, P., & Ma, X. (2014). Graphene–poly (vinyl alcohol) composites: Fabrication, adsorption and electrochemical properties. *Applied Surface Science, 314*, 815–821. https://doi.org/10.1016/j.apsusc.2014.07.075

Wang, Q. H., Li, M., Zheng, Z., Niu, Y., Xue, X. L., Ao, C. H., et al. (2022a). Polyethylenimine-functionalized nanofiber nonwovens electrospun from cotton cellulose for wound dressing with high drug loading and sustained release properties. *Polymers, 14*(9), 1748. https://doi.org/10.3390/polym14091748

Wang, S. W., Yu, Z. Y., He, Y. M., Li, C., Wang, L. L., & Wu, M. H. (2023). A fabric-based electrode for wearable piezoelectric nanogenerators to distinguish sense human motions. *Applied Surface Science, 610*, Article 155451. https://doi.org/10.1016/j.apsusc.2022.155451

Wang, X. Y., Xie, P. B., He, L., Liang, Y. W., Zhang, L., Miao, Y. Y., et al. (2022b). Ultralight, mechanically enhanced, and thermally improved graphene-cellulose-polyethyleneimine aerogels for the adsorption of anionic and cationic dyes. *Nanomaterials, 12*(10), 1727. https://doi.org/10.3390/nano12101727

Weerasundara, L., Gabriele, B., Figoli, A., Ok, Y.-S., & Bundschuh, J. (2021). Hydrogels: Novel materials for contaminant removal in water—A review. *Critical Reviews in Environmental Science and Technology, 51*(17), 1970–2014. https://doi.org/10.1080/10643389.2020.1776055

Wei, P., Wang, L., Xie, F., & Cai, J. (2022). Strong and tough cellulose–graphene oxide composite hydrogels by multi-modulus components strategy as photothermal antibacterial platform. *Chemical Engineering Journal, 431*, Article 133964. https://doi.org/10.1016/j.cej.2021.133964

Wei, X., Huang, T., Yang, J.-h., Zhang, N., Wang, Y., & Zhou, Z.-w. (2017). Green synthesis of hybrid graphene oxide/microcrystalline cellulose aerogels and their use as superabsorbents. *The Journal of Hazardous Materials, 335*, 28–38. https://doi.org/10.1016/j.jhazmat.2017.04.030

Wu, H., Tufa, L. T., Kwon, J., Choi, Y., & Lee, J. B. (2023). Facile one-pot synthesis of polyethyleneimine functionalized alpha-FeOOH nanoraft consisted of single-layer parallel-aligned ultrathin nanowires for efficient removal of Cr (VI): Synergy of reduction and adsorption. *Science of the Total Environment*, 857. https://doi.org/10.1016/j.scitotenv.2022.159446

Wu, S., Li, G., Liu, W., Yu, D., Li, G., Liu, X., et al. (2022). Fabrication of polyethyleneimine-paper composites with improved tribopositivity for triboelectric nanogenerators. *Nano Energy, 93*, Article 106859. https://doi.org/10.1016/j.nanoen.2021.106859

Yan, B., He, C., Chen, S., Xiang, L., Gong, L., Gu, Y., et al. (2022). Nanoconfining cation-π interactions as a modular strategy to construct injectable self-healing hydrogel. *CCS Chemistry, 4*(8), 2724–2737. https://doi.org/10.31635/ccschem.021.202101274

Yao, Z., Ge, L., Yang, W., Xia, M., Ji, X., Jin, M., et al. (2015). Finite dilution inverse gas chromatography as a versatile tool to determine the surface properties of biofillers for plastic composite applications. *Analytical Chemistry, 87*(13), 6724–6729. https://doi.org/10.1021/acs.analchem.5b01004

Yap, P. L., Nine, M. J., Hassan, K., Tung, T. T., Tran, D. N. H., & Losic, D. (2020). Graphene-based sorbents for multipollutants removal in water: A review of recent progress. *Advanced Functional Materials, 31*(9), Article 2007356. https://doi.org/10.1002/adfm.202007356

Yu, Y., Liang, Y., Zhang, Y., Xie, Z., Chen, J., Zheng, Z., et al. (2022). Characterizations and performances of polysulfone/graphene oxide with structural defects repaired by cellulose nanocrystals. *Polymer Composites, 43*(6), 3446–3456. https://doi.org/10.1002/pc.26627

Yun, H., Jung, S., Choi, J., Cho, S. Y., & Kwak, H. W. (2024). Highly efficient sorbent utilizing regenerated cellulose as an eco-friendly template for humic acid removal and oil–water separation processes. *Separation and Purification Technology, 341*, Article 126812. https://doi.org/10.1016/j.seppur.2024.126812

Zhang, E., Yang, J., & Liu, W. (2018). Cellulose-based hydrogels with controllable electrical and mechanical properties. *Zeitschrift für Physikalische Chemie, 232*(9–11), 1707–1716. https://doi.org/10.1515/zpch-2018-1133

Zhang, N., Zang, G.-L., Shi, C., Yu, H.-Q., & Sheng, G.-P. (2016). A novel adsorbent TEMPO-mediated oxidized cellulose nanofibrils modified with PEI: Preparation, characterization, and application for Cu (II) removal. *Journal of Hazardous Materials, 316*, 11–18. https://doi.org/10.1016/j.jhazmat.2016.05.018

Zhang, T., Xiao, S., Fan, K., He, H., & Qin, Z. (2022a). Preparation and adsorption properties of green cellulose-based composite aerogel with selective adsorption of methylene blue. *Polymer, 258*, Article 125320. https://doi.org/10.1016/j.polymer.2022.125320

Zhang, W. H., Wang, L. Y., Makila, E., Willfor, S., & Xu, C. L. (2022b). Ultralight and porous cellulose nanofibers/polyethyleneimine composite aerogels with exceptional performance for selective anionic dye adsorption. *Industrial Crops and Products, 177*, Article 114513. https://doi.org/10.1016/j.indcrop.2021.114513

Zhao, Z., Zhang, L., Song, Y., Ma, L., Li, J., Zhao, M., et al. (2023). Graphene oxide/styrene-butadiene latex hybrid aerogel with improved mechanical properties by PEI grafted GO and CNT. *Gels, 9*(5), 419. https://doi.org/10.3390/gels9050419

Zheng, X., Sun, W., Li, A., Wang, B., Jiang, R., Song, Z., et al. (2021). Graphene oxide and polyethyleneimine cooperative construct ionic imprinted cellulose nanocrystal aerogel for selective adsorption of Dy(III). *Cellulose, 29*(1), 469–481. https://doi.org/10.3390/gels9050419

Zhou, Y., Jin, Q., Hu, X., Zhang, Q., & Ma, T. (2012). Heavy metal ions and organic dyes removal from water by cellulose modified with maleic anhydride. *Journal of Materials Science, 47*, 5019–5029. https://doi.org/10.1007/s10853-012-6378-2